Ternary representation of contextual information along the CA1 transverse axis

Ya-Li Duan[1,3,4], Shu-Yi Hu[1,3,4], Xiao-Fan Ge[1,2], Jia-Li Long[1,3], Chu Deng[1,3], Yu-Ming Sun[1,3], Cheng-Ji Li[1,2], Rong Zhang[1,2], Xing Cai[1,2] & Li Lu[1,2,5]

1. Key Laboratory of Genetic Evolution & Animal Models, and Key Laboratory of Animal Models & Human Disease Mechanisms of Yunnan Province, Kunming Institute of Zoology, Chinese Academy of Sciences, Kunming, Yunnan 650201, China
2. National Research Facility for Phenotypic & Genetic Analysis of Model Animals (Primate Facility), Kunming Institute of Zoology, Chinese Academy of Sciences, Kunming, Yunnan 650107, China
3. Kunming College of Life Science, University of Chinese Academy of Sciences, Kunming, Yunnan 650204, China
4. Equal contribution
5. Corresponding author

Abstract

The CA1 region in the rat hippocampus exhibits a transverse organization, aligning with topographical input profiles from the entorhinal cortex and CA3-CA2 regions. This study investigated how CA1 neurons respond to various contextual changes along the transverse axis. Neuronal activity was monitored across the entire proximodistal extent of the CA1 region in Long-Evans rats under manipulations of spatial or non-spatial environmental cues. Results identified three distinct patterns of cue representation that varied from the proximal to distal end of the CA1 region: a descending gradient in spatial information processing, an ascending gradient in the representation of local object features, and a reverse J-shaped pattern in response to non-spatial cue manipulation. These heterogeneous patterns of neuronal activity are mutually independent, and closely linked to the nature of information altered in the environment, suggesting the involvement of upstream cue-selective neurons in shaping the function of the CA1 region.

Keywords:

CA1, transverse axis, remapping, spatial context, non-spatial cues, object

Introduction

The hippocampus plays a pivotal role in spatial navigation and episodic memory. In rodents, the collective localized firing of hippocampal neurons, known as place cells, generates a cognitive map of the spatial environment and provides a framework for associating episodic memories[1]. The hippocampus also creates distinct representations within populations of place cells to reflect changes in the internal state or external environment[2]. The place cell system employs discrete population codes to orthogonalize activity patterns in response to significant alterations in spatial context, known as global remapping. Conversely, it maintains the same population code for a given space but redistributes firing rates to distinguish non-spatial differences, such as color, odor, and motivation, a process termed rate remapping[3]. Place cell activity is modulated by inputs from surrounding brain regions, particularly the entorhinal cortex (EC), integrating multimodal sensory information and conveying highly processed signals to the hippocampus[4]. The medial EC (MEC) contains several specialized cell types, including grid cells[5], aperiodic spatial cells[6], head direction cells[7], border cells[8], and speed cells[9], which together form a dynamic representation of an animal's spatial location[10, 11]. In contrast, the lateral EC (LEC) exhibits minimal spatial selectivity in open fields[12, 13], with most neurons representing non-spatial features of the animal's experience, such as objects[14, 15], odors[16, 17], time[18], and egocentric position relative to landmarks[19], providing the hippocampus with a temporal progression of events[1]. Spatial and non-spatial information is processed separately within the MEC and LEC[20], thus potentially influencing the activity of hippocampal neurons through distinct MEC and LEC input pathways.

Divergent inputs from the EC converge at both the early and later stages of the hippocampal circuit through different pathways. Projections from layer II of the MEC and LEC terminate on distinct dendritic segments of individual neurons in the dentate gyrus (DG), distal CA3 (dCA3, near CA2), and CA2 regions. Medial and lateral fibers from layer III of the EC predominantly terminate on separate cell populations at different positions along the transverse axis of the CA1 and subiculum regions. MEC neurons preferentially project to the proximal CA1 (pCA1), near CA2, and the distal subiculum, distant from CA1, while LEC neurons primarily target the distal

CA1 (dCA1) and adjacent proximal subiculum[21, 22]. Additionally, MEC axons innervate a greater number of neurons in the deep CA1 pyramidal cell layer, whereas LEC fibers predominantly excite superficial CA1 pyramidal neurons[23]. Within the hippocampus, mossy fiber inputs from the DG decrease, and recurrent excitatory connections increase along the CA3-to-CA2 axis. The proximal CA3 (pCA3, engulfed by the DG) preferentially projects to dCA1, while dCA3/CA2 fibers primarily terminate at the neighboring pCA1. Pyramidal neurons in pCA1 and dCA1, in turn, project their axons to the distal and proximal subiculum, respectively. Ultimately, the CA1 and subiculum, as major output regions of the hippocampus, send reciprocal projections to the deep layers of the EC[21].

Distinct signals from the MEC and LEC[20], in conjunction with the topographically organized intrinsic and extrinsic hippocampal connections[21], result in functional segregation along the proximodistal axis of the hippocampus. Analyses of immediate-early gene expression patterns have identified subnetworks with distinct mnemonic functions along the transverse axis. The pCA3-dCA1 network preferentially processes non-spatial information, such as time, odor, and objects, across various behavioral tasks, while the dCA3-pCA1 network is more engaged in tasks requiring spatial memory[24-29]. Electrophysiological recordings have revealed a gradient in spatial representation along the transverse axis of the hippocampus, with stronger spatial tuning in pCA3 and pCA1 compared to dCA3/CA2 and dCA1[30-33], a more coherent response to conflicting local and global cues in dCA1 than in pCA1[34], and a decreased sensitivity to contextual changes or conflicting cues along the CA3-to-CA2 axis[31, 32]. Furthermore, recordings from multiple brain regions have highlighted the importance of coordinated ensemble activity between the LEC and dCA1 in odor-associated memory[16, 35]. Despite these insights, the specific manner in which CA1 neurons respond to contextual changes along the transverse axis and the degree to which selective inputs from upstream brain regions influence their activity remain unclear. To address these questions, we manipulated spatial, color, and object cues in the recording environment and compared changes in place cell ensemble activity across the entire proximodistal extent of CA1.

Results

Recording positions

A total of 15 rats were implanted with tetrodes targeting the right hippocampus. An additional five rats from a prior study[32] contributed proximal-to-middle CA1 data for the color-reversal and two-room tasks. Most recording sites were concentrated in the dorsal one-third of the hippocampus, with the collective dataset covering the entire proximodistal extent of the CA1 region (Fig. 1a). To facilitate cross-animal comparisons, recording positions were normalized for each tetrode, and the CA1 region was divided into three equal sized bands, with the following distribution: 39 tetrodes in the proximal band (pCA1), 43 in the middle band (mCA1), and 31 in the distal band (dCA1) (Supplementary Fig. 1).

Decreased spatial tuning from pCA1 to dCA1

The animals were initially trained and tested in the color-reversal task, involving the navigation of a square box with alternating black or white walls to find scattered cookie crumbs. A total of 178 experiments were conducted with 20 animals. Mean running speed decreased gradually across the four trials (Supplementary Fig. 2a), consistent with previous observations[15, 36]. Data analysis yielded 4 218 well-isolated, putative CA1 pyramidal neurons across 113 tetrodes, with 3 034 neurons demonstrating activity within the recording box (mean firing rate exceeding 0.1 Hz). The proportion of active cells diminished along the transverse axis of the CA1 region (Supplementary Fig. 2b). A total of 2 622 neurons with spatial information scores above the 95th percentile of the shuffled distribution were classified as place cells (Supplementary Fig. 2c,d) and selected for further analysis. While most active cells in CA1 displayed localized firing, a significantly higher proportion of place cells was observed in the proximal two-thirds of CA1 relative to dCA1 (Supplementary Fig. 2b).

We initiated our analyses by confirming the variance in position coding among CA1 subregions. Examination of place cell activity maps revealed that pCA1 contained cells with sharper and fewer place fields (Fig. 1b). A significant divergence in peak firing rates was noted across subcompartments (median (25%–75% percentile), pCA1, 5.327 (3.103–8.262) Hz, mCA1,

4.948 (3.065–7.411) Hz, and dCA1, 4.660 (2.854–7.407) Hz; Kruskal-Wallis test, 2 622 cells; H = 11.566, $P = 0.003$, Fig. 1c), although mean firing rates remained consistent (Supplementary Fig. 2e). Place cells in dCA1 contained significantly more place fields compared to cells in the proximal two-thirds of CA1 (pCA1, 1.00 (1.00–1.50), mCA1, 1.00 (1.00–1.50), and dCA1, 1.25 (1.00–1.75); H = 28.040, $P < 0.001$, Fig. 1d), yet the overall firing field size remained unchanged across subregions (Supplementary Fig. 2f). Place cells in pCA1 showed enhanced theta modulation (pCA1: 0.434 (0.333–0.540), mCA1: 0.410 (0.318–0.516), and dCA1: 0.390 (0.290–0.494); H = 28.301, $P < 0.001$, Fig. 1e) and a greater degree of phase locking to theta oscillations (Supplementary Fig. 2g) than cells located more distally. Furthermore, pCA1 cells exhibited higher spatial information content (pCA1: 2.037 (1.565–2.560) bits/spike, mCA1: 1.995 (1.508–2.540) bits/spike, and dCA1: 1.877 (1.454–2.429) bits/spike; H = 13.350, $P = 0.001$, Fig. 1f), spatial information rate (Supplementary Fig. S2h), coherence (pCA1: 0.656 (0.546–0.757), mCA1: 0.664 (0.553–0.758), and dCA1: 0.630 (0.507–0.715); H = 34.163, $P < 0.001$, Fig. 1g), and stability (pCA1: 0.741 (0.590–0.836), mCA1: 0.711 (0.583–0.814), and dCA1: 0.659 (0.521–0.769); H = 69.309, $P < 0.001$, Fig. 1h) than dCA1 cells. The observed variations in spatial tuning were not attributed to the dorsoventral distribution of recording sites, as cells recorded from the same transverse block of CA1 displayed a similar trend along the proximodistal axis (Supplementary Fig. 2i). To confirm the proximodistal gradient in spatial tuning, a naïve Bayes decoder was trained to predict the rat's location based on place cell population activity (Supplementary Fig. 2j). Decoding accuracy was ensured by analyzing only experiments with over 30 place cells in each subregion. Proximally located cells demonstrated superior prediction accuracy compared to simultaneously recorded distal cells (Supplementary Fig. 2k), indicating stronger position coding at pCA1.

To chart the decline in spatial tuning across the CA1 transverse axis, mean values for each measure were plotted against the tetrode location. Except for the number of place fields, all activity measures that varied across CA1 subregions exhibited a significant monotonic decline from the proximal to distal end of CA1. This pattern was substantiated by strong Pearson correlations between parameters and normalized recording position (all $P \leq 0.002$, 113 tetrodes). This decline was primarily linear, with minimal improvement in explained variance from

quadratic polynomial curve fitting (Fig. 1i–n and Supplementary Fig. 2l,m). Collectively, these findings demonstrate a gradual decline in spatial tuning from pCA1 to dCA1, consistent with previous reports[30, 33], and align with the selective spatial and non-spatial inputs from the MEC and LEC[22].

Reverse J-shaped rate remapping along transverse axis

Using the same dataset, we next investigated whether CA1 place cells displayed similar heterogeneity in response to non-spatial changes along the transverse axis. Rate remapping, characterized by alterations in firing rates within place fields while maintaining consistent firing locations[3], is indicative of sensitivity to contextual changes. As anticipated from prior work[32, 37, 38], rate remapping was induced in all 20 rats subjected to the color-reversal task (Supplementary Fig. 2n).

To assess the consistency of place field location across trials, the spatial correlation (SC) of rate maps was calculated to quantify the similarity in activity patterns of the same cell. SC scores were high for matching conditions but varied significantly across CA1 subregions (Fig. 2a left panel, two-way repeated-measures ANOVA, band: $F(2, 2\,619) = 26.679$, $P < 0.001$). SC decreased moderately between color-reversed conditions compared to matching conditions (color: $F(1, 2\,619) = 262.113$, $P < 0.001$), indicating adjustments in firing patterns in response to different colors. A significant band-color interaction was observed in SC ($F(2, 2\,619) = 28.724$, $P < 0.001$). The reduction in SC due to color change differed significantly across subregions (pCA1: 0.032 (−0.003–0.106), mCA1: 0.010 (−0.020–0.049), and dCA1: 0.025 (−0.011–0.091); Kruskal-Wallis test, 2 622 cells, $H = 68.492$, $P < 0.001$), with *post hoc* analysis revealing a nonlinear change in firing patterns along the proximodistal axis, with larger differences in pCA1 and dCA1 compared to mCA1 (Fig. 2a right panel; Holm-Bonferroni *post hoc* tests, both $P < 0.001$). Separate analyses for tetrodes located in the proximal or distal half of the axis showed significant correlations in both halves for SC (proximal: $r = -0.375$, $P = 0.002$, Pearson correlation, 63 tetrodes; distal: $r = 0.374$, $P = 0.007$, 50 tetrodes). The changes in SC along the entire CA1 transverse were better explained by quadratic polynomial curve fitting (Fig. 2b).

To quantify the extent of rate remapping, the rate difference (RD) was calculated, representing the normalized overall change in firing rate for each cell. Consistent with the observed SC pattern, mCA1 contained the smallest proportion of strongly rate-remapped place cells between different colors (Supplementary Fig. 2o). The RD differed significantly between condition pairs and across CA1 subregions (Fig. 2c left panel, color: $F(1, 2\,619) = 288.514$, $P < 0.001$; band: $F(2, 2\,619) = 20.373$, $P < 0.001$). There was a significant interaction between CA1 band and color in RD ($F(2, 2\,619) = 41.298$, $P < 0.001$), along with regional variations in elevated RD between condition pairs (Fig. 2c right panel, pCA1: 0.012 (−0.005–0.140), mCA1: 0.001 (−0.006–0.047), and dCA1: 0.001 (−0.010–0.048); $H = 38.540$, $P < 0.001$). Cells in both pCA1 and dCA1 exhibited more pronounced rate redistribution than those in mCA1 when the wall color was reversed, with pCA1 showing a significantly greater increase in RD between condition pairs (*post hoc* tests, both $P < 0.001$). Mean changes in RD for individual tetrodes were significantly correlated with recording position in both the proximal and distal halves of the CA1 transverse axis (proximal: $r = -0.452$, $P < 0.001$; distal: $r = 0.314$, $P = 0.029$, Fig. 2d). A similar result was obtained when the RD for individual place fields were computed and summed according to their weight (Supplementary Fig. 2p–s), indicating that the lower rate changes in the middle-to-distal CA1 were not due to neutralization of individually remapped place fields.

To compare activity changes in cell assemblies across CA1 subregions, the population vector correlation (PVC) was computed for all recorded pyramidal neurons, including non-place cells and inactive cells. PVC is sensitive to the composite distribution of firing location and rate [37]. Results showed that population vectors (PVs) from corresponding locations in the box were strongly correlated between matching conditions in all CA1 subregions. However, the correlations were weaker between black and white configurations (Fig. 2e,f). Differences in PVC between conditions with reversed wall colors and conditions with matching wall colors were significant across subregions (color: $F(1, 1\,197) = 3\,336.027$, $P < 0.001$; band: $F(2, 1\,197) = 396.174$, $P < 0.001$; color × band: $F(2, 1\,197) = 448.356$, $P < 0.001$, Fig. 2e left panel). mCA1 exhibited the smallest change in PVC between condition pairs (pCA1: 0.108 (0.085–

0.147), mCA1: 0.031 (0.005–0.054), and dCA1: 0.052 (0.022–0.094); H = 541.211, $P < 0.001$, 1 200 bins, *post hoc* tests, all $P < 0.001$, Fig. 2e right panel).

A pronounced hysteresis effect was observed in all CA1 subregions in the color-reversal task. Activity patterns were more similar between trials 3 and 4 than between trials 1 and 2, despite both involving black and white configurations (Supplementary Fig. 2t). To avoid the carryover effect in the analyses, data from the 1-2 trial pair (different color) and 2-3 trial pair (same color) were compared, yielding similar results (data not shown). To verify the reverse J-shaped pattern of rate remapping along the CA1 transverse axis, a naïve Bayes decoder was trained with collective activities of place cells in trials 2 and 3 (white walls), predicting the rat's location in trial 1 (black walls). For the three experiments with over 30 simultaneously recorded place cells in both subregions, decoding accuracy was higher in the mCA1 subregion than in the other two CA1 subregions (Supplementary Fig. 2u), indicating minimal activity change in mCA1 between the black and white configurations. In summary, in the color-reversal task, which evoked rate remapping in the hippocampus, the rate distribution varied significantly along the transverse axis of CA1, with robust redistribution of firing rates in pCA1, moderate redistribution in dCA1, and minimal redistribution in mCA1.

Graded global remapping along the proximodistal axis

We further investigated whether the gradient in spatial tuning along the CA1 proximodistal axis would similarly exhibit a monotonic decrease in global remapping. In a second set of experiments, pyramidal neurons were recorded from the same 20 rats as they were tested in similar square boxes situated in two distinct rooms, a paradigm known to trigger global remapping in the hippocampus[32, 37]. Of the 19 rats from which valid place cell data were obtained, 13 displayed clear global remapping, characterized by minimal correlation in firing fields between rooms, while the remaining six exhibited extensive rate remapping (Supplementary Fig. 3a). These individual differences align with previous studies[32, 38]. The results from the six rate-remapped animals were consistent with findings from the color-reversal task (Supplementary Fig. 3b–f). Further analysis focused on the 13 globally remapped rats, which demonstrated comparable behavior in the two-room task to that in the color-reversal

task (Supplementary Fig. 3g). A total of 1 145 pyramidal neurons were recorded from 54 tetrodes, with 761 identified as place cells. As anticipated, a similar decrease in activity measures along the CA1 transverse axis was observed in these rats (Supplementary Fig. 3h–q).

Global remapping, characterized by the engagement of a second population of place cells to represent a distinct spatial map in the hippocampus[3], was evident at the individual cell level based on significant changes in the firing location and rate within the recording box (Fig. 3a). The degree of population overlap was consistent across CA1 subregions (Supplementary Fig. 3r). The SC of individual place cells between repeated trials in the same room remained high for all CA1 subregions and decreased markedly between rooms (two-way repeated-measures ANOVA, room: F (1, 758) = 1 175.415, $P < 0.001$, Fig. 3b, left panel), indicating substantial shifts in firing location across different rooms. Between-room SC showed a tendency to be higher in both mCA1 and dCA1 (band: F (2, 758) = 13.538, $P < 0.001$, Supplementary Fig. 3s). A pronounced room-band interaction in SC was observed (F (2, 758) = 27.266, $P < 0.001$). The reduction in SC in response to room change decreased progressively along the proximodistal axis of CA1 (pCA1, 0.455 (0.256–0.747), mCA1, 0.354 (0.151–0.527), and dCA1, 0.287 (0.095–0.504); Kruskal-Wallis test, 761 cells, H = 41.735, $P < 0.001$), with the most significant changes occurring in pCA1 (Holm-Bonferroni *post hoc* tests, pCA1 vs mCA1, pCA1 vs dCA1, both $P < 0.001$), suggesting the largest shift in place field location in this subregion. The difference in SC decrease was not attributed to variations in sample size (Supplementary Fig. 3t). The decline in SC for each tetrode was strongly correlated with its position along the CA1 transverse axis (Fig. 3c).

The overall firing rate within the room is indicative of the activity level of individual neurons. A similar monotonic decrease in firing rate change was observed along the proximodistal axis. The RD remained low for repeated trials in the same room across all subregions but increased markedly between trials conducted in different rooms (room: F (1, 758) = 410.559, $P < 0.001$; band: F (2, 758) = 0.380, $P = 0.684$). This enhancement in RD between condition pairs was strongly dependent on the subregion (room × band: F (2, 758) = 23.136, $P < 0.001$), with the greatest increase observed in pCA1 (pCA1, 0.261 (0.034–0.484), mCA1, 0.082 (0–0.352), and

dCA1, 0.073 (−0.003–0.274); H = 39.143, $P < 0.001$; *post hoc* tests, pCA1 vs mCA1, pCA1 vs dCA1, both $P < 0.001$, Fig. 3d), suggesting greater interdependent activity in the distal two-thirds of the CA1 region across different rooms. The varied increase in RD was not due to variations in sample size (Supplementary Fig. 3u). A significant correlation was also observed between the change in RD and recording position (Fig 3e).

Next, ensemble coding across CA1 subregions was compared. Unlike the color-reversal task, the effect of hysteresis was minimal in the two-room task (Supplementary Fig. 3v). Correlations between corresponding PVs were high for trials within the same room across all subregions but decreased substantially between trials in different rooms (room: F (1, 1 197) = 28 489.675, $P <$ 0.001; band: F (2, 1 197) = 83.437, $P < 0.001$). The reduction in PVC was region-dependent (room × band: F (2, 1 197) = 800.992, $P < 0.001$), with pCA1 exhibiting the greatest decrease (0.678 (0.609–0.731)), mCA1 showing a moderate decrease (0.452 (0.367–0.535)), and dCA1 demonstrating the smallest decrease (0.388 (0.334–0.441); H = 679.871, $P < 0.001$, 1 200 bins; *post hoc* tests, all $P < 0.001$, Fig. 3f,g). In summary, when global remapping was induced in the hippocampus by distinct spatial environments, the representations of place cells were most orthogonal in pCA1, with the degree of orthogonalization decreasing monotonically along the transverse axis.

Given that greater independent ensemble coding across rooms coincided with increased spatial modulation in pCA1, we further explored the potential relationship between these phenomena. Analysis revealed that the spatial information scores of CA1 place cells active in both rooms were not significantly different (1.799 (1.377–2.354) vs 1.776 (1.334–2.352), Wilcoxon signed-rank test, 483 cells, Z = −1.161, $P = 0.246$) and exhibited a strong correlation (Fig. 3h), indicating consistent spatial information processing within individual place cells, regardless of the spatial environment. Furthermore, the mean spatial information scores across the four trials were significantly correlated with variations in SC and RD between the two rooms (Fig. 3i,j). Consistent results were observed using alternative spatial tuning measures at both the cellular and tetrode levels (Supplementary Fig. 3w–z). These findings corroborate the relationship between reduced orthogonalization and decreased spatial modulation along the CA1 transverse

axis, implying that spatial information input to distinct CA1 subregions influences both patterns.

Reorganized CA1 population activity in object-placement task

Hippocampal place cell activity is influenced by discrete objects within an open arena, as documented in previous reports[39-42]. In a third set of experiments, we investigated whether the response to familiar objects in CA1 varied by region. Place cell activity was recorded from 14 rats during the object-placement task, in which two identical familiar objects were introduced to the recording box in trials 2 and 3 of the four-trial experiment (Supplementary Fig. 4a). Despite no significant change in overall behavior in response to the objects, alterations in theta and low-beta power were noted, potentially linked to exploratory behavior (Supplementary Fig. 4b–d). A total of 1 759 active place cells were identified from 2 711 putative pyramidal neurons recorded across 72 tetrodes in 65 experiments (Supplementary Fig. 4e). A substantial subset of place cells responded to the object placement, primarily by redistributing their firing rates around the objects (Fig. 4a). The dCA1 region exhibited the highest proportion of cells that altered their number of receptive fields (pCA1, 40.88%, mCA1, 41.42%, and dCA1, 49.93%; chi-square test, $\chi^2 = 12.777$, $P = 0.002$; *post hoc* tests, mCA1 vs dCA1, $P = 0.004$; pCA1 vs dCA1, $P = 0.019$), while the mCA1 subregion showed the highest proportion of stable cells (Fig. 4b and Supplementary Fig. 4f). A pronounced hysteresis effect was observed in trial 4 of the object-placement task (Supplementary Fig. 4g), leading to the exclusion of trial 4 data from analyses to prevent carryover effects. Consequently, analyses focused on activity changes between trials 1 and 2 (before and after object placement) and between trials 2 and 3 (both with objects).

Given that hippocampal place cells collectively signal the presence of objects at a population level[40], all active place cells were included in our analyses. Upon the introduction of familiar objects, a uniform decrease in SC was observed across all subregions (Supplementary Fig. 4h, left panel). Furthermore, RD analyses revealed a slight overall increase in rate redistribution post-object placement, with the most significant changes occurring in pCA1 (Supplementary Fig. 4h, right panel). Unlike previous experiments, no significant correlation was found between changes in SC or RD and the recording position (Pearson correlations, 72 tetrodes, SC:

r = 0.213, P = 0.072, RD: r = 0.049, P = 0.681). Overall, PVCs were high for trials under matching conditions but decreased significantly with object introduction (two-way repeated-measures ANOVA, object: F (1, 1 197) = 2 475.217, $P < 0.001$; band: F (2, 1197) = 182.697, $P < 0.001$). This decline in PVC was strongly dependent on the CA1 subregion (object × band: F (2, 1 197) = 11.762, $P < 0.001$), with the most pronounced reduction observed in pCA1 (pCA1, 0.121 (0.070–0.183), mCA1, 0.084 (0.037–0.157), and dCA1, 0.095 (0.050–0.158); Kruskal-Wallis test, 1 200 bins, H = 38.042, $P < 0.001$; Holm-Bonferroni *post hoc* tests, pCA1 vs mCA1, pCA1 vs dCA1, both $P < 0.001$, Fig. 4c,d). Bayesian decoding demonstrated significantly better prediction accuracy in mCA1 than in dCA1 (Supplementary Fig. 4i). Analysis of PVCs in each spatial bin revealed that most decreases in PVC were localized around the objects and diminished with distance, consistent with previous findings[40]. Additionally, dispersed activity changes away from the objects were observed in both pCA1 and dCA1, suggesting these responses were not directly related to the presence of the objects.

To further characterize the activity changes induced by object placement, we defined an object region compassing the area within 20 cm of the center of each object. This enabled the comparison of direct and indirect object responses by quantifying spatial bins inside and outside the target region. Although dCA1 place cells exhibited the lowest SC and highest RD scores within the object region after object placement, the changes in SC and RD between trial pairs were not significantly different across CA1 subregions (SC: object, F (1, 1 196) = 271.560, $P < 0.001$; band, F (2, 1 196) = 12.690, $P < 0.001$; object × band, F (2, 1 196) = 1.599, P = 0.203. RD: object, F (1, 1 756) = 198.557, $P < 0.001$; band, F (2, 1 756) = 17.791, $P < 0.001$; object × band, F (2, 1 756) = 0.210, P = 0.811). Population analysis of bins within the object region demonstrated significant regional differences across CA1 subregions (object: F (1, 237) = 2262.040, $P < 0.001$; band: F (2, 237) = 96.016, $P < 0.001$; object × band: F (2, 237) = 4.720, P = 0.010), with a slightly higher PVC decrease in mCA1 than in dCA1 (pCA1, 0.199 (0.171–0.228), mCA1, 0.215 (0.174–0.285), and dCA1, 0.185 (0.154–0.239); H = 7.232, P = 0.027, 240 bins, *post hoc* tests, mCA1 vs dCA1, P = 0.034; Fig. 4e).

Outside the object region, CA1 place cells consistently exhibited a decrease in SC across

361 subregions between trial pairs (object, F (1, 1 439) = 216.332, $P < 0.001$; band, F (2, 1 439) =
362 31.664, $P < 0.001$; object × band, F (2, 1 439) = 2.032, $P = 0.131$; Fig. 4f top). Cells in mCA1
363 displayed minimal changes in firing rate following object placement, similar to rate remapping
364 (RD: object, F (1, 1 756) = 168.577, $P < 0.001$; band, F (2, 1 756) = 12.823, $P < 0.001$; object
365 × band, F (2, 1 756) = 4.189, $P = 0.015$). The increase in RD between conditions varied
366 significantly across CA1 subregions (pCA1, 0.080 (−0.037–0.275), mCA1, 0.033 (−0.059–
367 0.192), and dCA1, 0.062 (−0.087–0.244); H = 9.868, $P = 0.007$, 1 759 cells, *post hoc* tests,
368 pCA1 vs dCA1, $P = 0.064$, pCA1 vs mCA1, $P = 0.005$; Fig. 4f middle), but was not related to
369 sample size or exploratory behavior around the objects (Supplementary Fig. 4j,k). Population
370 analysis indicated a PVC distribution pattern resembling rate remapping after object placement
371 along the CA1 transverse axis (object: F (1, 957) = 2 043.235, $P < 0.001$; band: F (2, 957) =
372 221.229, $P < 0.001$; object × band: F (2, 957) = 32.592, $P < 0.001$), and a reverse J-shaped
373 change in PVC between trial pairs (pCA1, 0.096 (0.065–0.150), mCA1, 0.063 (0.026–0.107),
374 dCA1, 0.075 (0.042–0.130); H = 66.740, $P < 0.001$, 960 bins; *post hoc* tests, all $P \leq 0.004$; Fig.
375 4f bottom).
376
377 In summary, the introduction of familiar objects into the open box elicited both direct and
378 indirect responses in the CA1 region. The direct response led to changes in population activity
379 primarily around the objects, whereas the indirect response was more evident away from the
380 objects. Neurons in mCA1 showed the strongest local response to the objects but the weakest
381 overall reorganization of population activity, likely due to greater rate redistributions outside
382 the object region in pCA1 and dCA1.
383
384 **Ascendant response to translocated object from pCA1 to dCA1**
385 Given the critical role of the hippocampus and MEC in object-location memory, as evidenced
386 by deficits following damage to these areas[43], we investigated whether the presentation of object
387 location in CA1 exhibited a gradient along the proximodistal axis, similar to spatial tuning. In
388 a fourth set of experiments, the same 14 rats participated in the object-relocation task, where a
389 familiar object was moved from its original location in quadrant 4 to quadrant 1 of the recording
390 box (Supplementary Fig. 5a,b). Despite variations in individual responses to object

translocation, the overall discrimination index remained unchanged (Supplementary Fig. 5c). Exploration around the displaced object was accompanied by minor fluctuations in theta and low-beta power, with regional differences observed at 8–9 and 14–15 Hz (Supplementary Fig. 5d). A total of 2 367 putative pyramidal neurons were recorded across 69 tetrodes in 59 experiments, of which 1 486 were identified as active place cells (Supplementary Fig. 5e). A substantial subset of CA1 place cells altered their firing patterns, primarily through changes in firing rate around the displaced object (Fig. 5a). Contrary to expectations, dCA1, rather than pCA1, exhibited the highest proportion of cells responsive to the translocation (pCA1, 63.88%, mCA1, 71.81%, and dCA1, 78.66%; chi-square test, $\chi^2 = 20.691$, $P < 0.001$; *post hoc* tests, pCA1 vs mCA1, $P = 0.081$; mCA1 vs dCA1, $P = 0.015$; pCA1 vs dCA1, $P < 0.001$; Fig. 5b). Due to hysteresis effects (Supplementary Fig. 5f), analyses focused on activity changes between trials 1 and 2 (before and after relocation) and between trials 2 and 3 (both with one relocated object).

The SC for individual place cells was high in matching trials but slightly reduced after object relocation across all CA1 subregions (two-way repeated-measures ANOVA, relocation: F (1, 1 483) = 153.986, $P < 0.001$; band: F (2, 1 483) = 21.400, $P < 0.001$). The reduction in SC varied significantly by subregion (relocation × band: F (2, 1 483) = 4.917, $P = 0.007$), with the smallest decrease in pCA1 (0.024 (−0.026–0.121)), a moderate reduction in mCA1 (0.049 (−0.021–0.175)), and the largest decrease in dCA1 (0.069 (−0.027–0.233); Kruskal-Wallis test, 1 486 cells, H = 10.123, $P = 0.006$; Holm-Bonferroni *post hoc* tests, pCA1 vs dCA1, $P = 0.005$, Fig. 5c). A significant correlation was observed between SC change and tetrode location (r = 0.347, $P = 0.004$, Pearson correlation, 69 tetrodes, Fig. 5d). The increase in RD between trial pairs mirrored the SC decrease across CA1 subregions (relocation: F (1, 1 483) = 147.858, $P < 0.001$; band: F (2, 1 483) = 20.702, $P < 0.001$), with a near-significant interaction between relocation and band (F (2, 1 483) = 2.609, $P = 0.074$). The elevation in RD between trial pairs increased progressively from pCA1 to dCA1 (pCA1, 0.044 (−0.073–0.205), mCA1, 0.057 (−0.057–0.221), and dCA1, 0.112 (−0.056–0.308); H = 9.346, $P = 0.009$; *post hoc* tests, pCA1 vs dCA1, mCA1 vs dCA1, both $P < 0.05$, Fig. 5e). A significant correlation was also found between the shift in RD for individual tetrodes and their recording position (r = 0.243, $P =$

0.044, Pearson correlation, 69 tetrodes, Fig. 5f). The graded changes in SC and RD were not influenced by exploratory behavior around the objects or by sample size (Supplementary Fig. 5g–i), with similar results obtained when rate changes were computed for individual place fields (Supplementary Fig. 5j,k).

Correlations between corresponding PVs in each spatial bin changed in a manner similar to the alterations observed in SC (relocation: F (1, 1 197) = 1 097.785, $P < 0.001$; band: F (2, 1 197) = 20.565, $P < 0.001$; relocation × band: F (2, 1 197) = 26.839, $P < 0.001$). The decline in PVC between trial pairs increased from pCA1 to dCA1 (pCA1, 0.055 (0.014–0.111), mCA1, 0.068 (0.030–0.127), dCA1, 0.077 (0.043–0.138); H = 44.493, $P < 0.001$, 1 200 bins; *post hoc* tests, pCA1 vs dCA1, pCA1 vs mCA1, both $P < 0.001$; mCA1 vs dCA1, $P = 0.063$, Fig. 5g). Bayesian decoding revealed significantly improved context predictions in regions located more proximally along the CA1 transverse axis (Supplementary Fig. 5l). Similar to the object-placement task, a substantial decrease in PVC was observed for bins around the right object before and after object displacement (Fig. 5h left). However, pCA1 exhibited the least degree of reorganization in activity pattern within the target region (pCA1, 0.081 (0.054–0.114), mCA1, 0.212 (0.147–0.269), and dCA1, 0.225 (0.155–0.303); H = 125.736, $P < 0.001$, 240 bins; *post hoc* tests, pCA1 vs dCA1, pCA1 vs mCA1, both $P < 0.001$; Fig. 5h and Supplementary Fig. 5m left). For spatial bins outside the target region, the change in PVC was minimal, and the linear proximodistal distribution differed from the reverse J-shaped distribution observed in the object-placement task (pCA1, 0.043 (0.009–0.106), mCA1, 0.049 (0.026–0.091), and dCA1, 0.063 (0.038–0.101); H = 17.077, $P < 0.001$, 960 bins; *post hoc* tests, pCA1 vs dCA1, mCA1 vs dCA1, both $P < 0.05$, Fig. 5h, Supplementary Fig. 4l and 5m right), suggesting that translocation of an existing object did not trigger a rate remapping-like indirect response in the CA1 region. In conclusion, the translocation of a single familiar object within the open arena led to more pronounced changes in ensemble activity around the object in the distal two-thirds of the CA1 region, with minimal changes outside the target region.

Enhanced rate redistribution to novel object from pCA1 to dCA1

Object-recognition memory, unlike object-location memory, is heavily dependent on the

451 perirhinal cortex (PER), which projects to the LEC and dCA1[21, 43], highlighting the importance
452 of the PER/LEC-dCA1 network in discriminating object identity. To determine whether
453 selective PER/LEC input to dCA1 creates a proximodistal gradient in place cell activity in
454 response to a novel object, the same 14 rats were tested using the novel-object task, where a
455 familiar object on the right was replaced by a novel object during trials 2 and 3 (Supplementary
456 Fig. 6a,b). Results indicated that the total exploration time around the novel object was
457 comparable to that of the familiar object, and there were no significant changes in theta and
458 low-beta power (Supplementary Fig. 6c,d). A total of 1 451 active place cells were identified
459 from 2 207 putative pyramidal neurons recorded across 67 tetrodes in 54 experiments. Unlike
460 previous tasks, which showed lower recruitment of place cells in dCA1 compared to pCA1, the
461 novel-object task exhibited similar activation of place cells across all CA1 subcompartments
462 (Supplementary Fig. 6e), consistent with the engagement of more dCA1 neurons upon exposure
463 to a novel object[27]. A substantial subset of place cells adjusted their firing rates in response to
464 the novel object (Fig. 6a), with dCA1 showing the highest proportion of identity-response cells
465 (pCA1, 53.38%, mCA1, 63.02%, and dCA1, 73.58%; chi-square test, $\chi^2 = 37.366$, $P < 0.001$;
466 *post hoc* tests, all $P \leq 0.021$; Fig. 6b). Given the minimal changes in ensemble activity between
467 trials 3 and 4 across all subregions (Supplementary Fig. 6f), our analyses focused on shifts in
468 firing rate between trials 1 and 2 (object identity switched) and between trials 2 and 3 (object
469 identity unchanged).
470
471 The SC scores of individual place cells remained high across all subregions under matching
472 conditions, with only a slight decrease after object replacement (two-way repeated-measures
473 ANOVA, novelty F (1, 1 448) = 69.447, $P < 0.001$; band: F (2, 1 448) = 21.964, $P < 0.001$). No
474 interaction between the CA1 band and novelty was observed (F (2, 1 448) = 0.528, $P = 0.590$),
475 indicating no regional differences in SC change between trial pairs (Fig. 6c). The overall
476 changes in firing rate for individual place cells were marginally but significantly enhanced in
477 trial pairs before and after object replacement (novelty F (1, 1 448) = 58.170, $P < 0.001$; band:
478 F (2, 1 448) = 10.527, $P < 0.001$), with the degree of enhancement strongly dependent on the
479 location of the place cells (novelty × band: F (2, 1 448) = 6.169, $P = 0.002$). Neurons in pCA1
480 exhibited the lowest increase in RD (0.008 (−0.101–0.120)), followed by mCA1 (0.036

481 (−0.064–0.162)) and dCA1 (0.054 (−0.085–0.225); Kruskal-Wallis test, 1 451 cells, H = 13.604,
482 P = 0.001; Holm-Bonferroni *post hoc* tests, both $P < 0.05$, Fig. 6d). The enhancement in RD
483 showed a significant correlation recording positions (r = 0.356, P = 0.003, Pearson correlation,
484 67 tetrodes, Fig. 6e). The graded changes in RD were not related to exploratory behavior around
485 objects or sample size (Supplementary Fig. 6g–i). Similar results were obtained for RD scores
486 calculated from individual place fields (Supplementary Fig. 6j,k).
487
488 The ensemble activity of all pyramidal neurons, as measured by PVC, demonstrated a marginal
489 decrease following object replacement (novelty: F (1, 1 197) = 1 388.100, $P < 0.001$; band: F
490 (2, 1 197) = 261.805, $P < 0.001$), with a significant interaction between novelty and CA1 band
491 (F (2, 1 197) = 12.330, $P < 0.001$). The smallest change in activity pattern in response to the
492 novel object was observed in cell assemblies within pCA1 (pCA1, 0.031 (0.006–0.065), mCA1,
493 0.040 (0.023–0.061), and dCA1, 0.047 (0.014–0.079); H = 19.995, $P < 0.001$, 1,200 bins; *post*
494 *hoc* tests, pCA1 vs. dCA1, pCA1 vs. mCA1, both $P \leq 0.007$, Fig. 6f). Bayesian decoding
495 indicated better context prediction for cells located in mCA1 compared to those in dCA1
496 (Supplementary Fig. 6l). Compared to the other two object-related tasks, the reorganization of
497 population activity in response to the novel object was less pronounced and less localized across
498 all CA1 subdivisions (Fig. 6g left panel). However, the regional variance in response to the
499 novel object was primarily attributed to subtle differences in activity changes around the object
500 (bins around novel object: pCA1, 0.005 (−0.014–0.028), mCA1, 0.034 (0.021–0.046), and
501 dCA1, 0.070 (0.053–0.082); H = 61.612, $P < 0.001$, 120 bins; *post hoc* tests, all $P \leq 0.001$), as
502 ensemble activity changes outside the object region remained largely constant across CA1
503 subregions (bins outside object region: pCA1, 0.035 (0.009–0.069), mCA1, 0.041 (0.023–
504 0.064), and dCA1, 0.044 (0.012–0.078); H = 5.689, P = 0.058, 1 080 bins; Fig. 6g and
505 Supplementary Fig. 6m). In conclusion, place cells located more distally along the CA1
506 transverse axis displayed greater firing rate redistribution around the novel object, likely due to
507 preferential inputs from object-identity cells in the LEC and PER[13, 14, 44, 45].
508
509 **Independent neuronal responses across cue manipulations**
510 In our final set of analyses, we investigated whether the heterogeneity patterns observed along

the CA1 transverse axis were influenced by correlated CA1 population activity during related tasks within the same spatial context. We focused on firing rate changes of individual CA1 place cells during tasks that elicited analogous proximodistal activity patterns. To ensure accurate identification of the same neurons across different experiments, we used a threshold of 0.6359 based on the 95th percentile value of SC from random permutation between spatial maps. Based on this criterion, 235 place cells from neighboring color-reversal and object-placement experiments and 267 place cells from neighboring object-relocation and novel-object experiments were identified. These task pairs induced comparable patterns of proximodistal heterogeneity in CA1 (Supplementary Fig. 7a,b).

Our analysis revealed that the activity patterns of individual neurons in the color-reversal and object-placement tasks were largely unrelated. Some neurons responded exclusively to cue changes in one task, while others altered their firing rates in both tasks, but with varying directions and intensities (Fig. 7a). Despite the similar degrees of firing rate changes induced by color-reversal and indirect responses to object-placement (two-way repeated-measures ANOVA, task: $F(1, 234) = 1.110$, $P = 0.293$; condition: $F(1, 234) = 27.221$, $P < 0.001$; task × condition: $F(1, 234) = 0.021$, $P = 0.886$, Fig. 7b), there was only partial overlap between the cell populations that responded to each type of cue manipulation. Cells with a RD score higher than 0.2 (equivalent to a 50% increase in firing rate, close to the median RD between matching conditions) showed an overlap that did not deviate from what would be expected by chance (binomial test, $Z = 0.226$, $P = 0.326$, Fig. 7c). Furthermore, no correlation was observed between variations in RD across the two tasks (Pearson correlation, $r = 0.007$, $P = 0.909$, Fig. 7d). Similar results were obtained when the overall RD, instead of the out-object-region RD, in the object-placement task was computed (Supplementary Fig. 7c,d). These findings suggest that although similar heterogeneity patterns were induced in both tasks, the neuronal responses were largely independent of one another.

In both the object-relocation and novel-object tasks, we observed diverse cellular responses to changes in object features (Fig. 7e). Changes in RD of these neurons did not differ significantly between the two tasks (task: $F(1, 266) = 2.847$, $P = 0.093$; condition: $F(1, 266) = 30.873$, $P <$

0.001; task × condition: F (1, 266) = 2.218, P = 0.138, Fig. 7f). The overlap in cell populations that responded to changes in object features was not significantly greater than what would be expected by chance (binomial test, Z = 0.232, P = 0.166, Fig. 7g). Additionally, variations in RD induced by changes in object location or identity were not significantly correlated (Pearson correlation, r = 0.094, P = 0.127, Fig. 7h). Similar findings were noted for cells active in both object-placement and object-relocation task pairs, as well as in the object-placement and novel-object task pairs (Supplementary Fig. 7e–l). To further substantiate the independence of neuronal responses to object features, we identified 122 place cells that were recorded across all three object-related tasks. The population overlaps between responsive cells in different tasks were at chance levels, and changes in RD across tasks were not correlated (Supplementary Fig. 7m,o). In conclusion, the hippocampal CA1 region demonstrated physically overlapping but functionally independent population coding for distinct cue manipulations within the same spatial environment, highlighting a causal relationship between the activities of distinct upstream functional neuronal populations and the downstream neuronal responses in hippocampal CA1.

Discussion

Our study provides a comprehensive characterization of how CA1 subcompartments in the rat hippocampus respond to various spatial and non-spatial modifications. We identified three distinct patterns of cue representation along the proximodistal axis of CA1 that may affect hippocampal output, including a gradient of decreasing spatial information processing, an increase in the representation of local object features, and most intriguingly, a reverse J-shaped response to non-spatial environmental changes. These population response patterns were largely independent of one another, possibly attributed to the distinct nature of contextual cues and their association with selective inputs from particular functional neuronal populations (Fig. 8)[10, 13-15, 19].

Entorhinal and CA3-CA2 projections serve as the primary afferent pathways to the CA1 region in rats (Fig. 8). Our findings support the established view that spatial tuning and global

remapping in the CA1 region exhibit a gradient decrease from the proximal to distal end (Fig. 1 & 3)[30, 33, 34]. Global remapping in the rat hippocampus is accompanied by a realignment of activity patterns in grid, head direction, and border cells within the MEC[8, 46]. This reorganization appears to minimize spatial information overlap, potentially enhancing distinct spatial representations in pCA1. In contrast, neurons in the LEC, which encode shared non-spatial features, may maintain their activity levels, contributing to more generalized ensemble activity in dCA1[29, 36]. The gradients in spatial selectivity and global remapping observed in the CA1 region can thus be attributed to differential inputs from the MEC and LEC, with pCA1 predominantly receiving spatial signals from the MEC and dCA1 primarily receiving non-spatial signals from the LEC[20].

A notable finding in our study is the discovery of a reverse J-shaped rate remapping pattern within CA1 in both the color-reversal and object-placement tasks (Fig. 2 & 4). The pronounced rate redistribution observed in both pCA1 and dCA1 suggests contributions from both the MEC and LEC to hippocampal rate coding. Certain LEC neurons are known to remap in response to contextual changes in the environment, and lesions in the LEC have been shown to partially impair rate coding in CA3[13, 38]. This finding supports the hypothesis that the LEC provides modulated non-spatial inputs critical for hippocampal rate remapping[47]. Conversely, MEC grid cells maintain consistent firing locations within the same spatial context but exhibit reliable rate redistribution in response to non-spatial manipulations[48-50]. Precise modulation of MEC activity has been linked to hippocampal remapping[51-53], indicating that rate redistribution in MEC cells may influence the firing rates of place cells. The weak rate remapping observed in mCA1 may be due to two potential causes: first, the signal integration process in mCA1 may differ from that in neighboring pCA1 and dCA1[54], although the linear gradients observed in other tasks argue against this possibility; second, the rate redistribution signals from the MEC and LEC may be mutually exclusive, suggesting a dynamic interplay between these inputs influences neuronal outputs in the CA1 region. We propose that the degree of rate remapping in CA1 may be determined by the relative dominance of MEC and LEC inputs along the transverse axis. Neurons in pCA1 or dCA1, which predominantly receive inputs from either the MEC or LEC, follow the dominant input and exhibit pronounced rate remapping. In contrast, mCA1 neurons,

which receive balanced inputs from both the MEC and LEC, display weaker rate remapping due to the competing influences.

The introduction of familiar objects elicited a robust direct response across all CA1 subcompartments (Fig. 4). Notably, the local changes in firing rate were not correlated with exploratory behaviors around the objects (Supplementary Fig. 4k), indicating limited involvement of investigatory intention-modulated hippocampal neurons[55]. Both the MEC and LEC contain neurons that respond to discrete objects in the environment, albeit within different reference frames[14, 19, 56]. Additionally, the PER, which projects to the LEC and dCA1, contains object-responsive cells similar to those found in the LEC[21, 44, 45]. These findings suggest that CA1 neurons may integrate signals from MEC object-vector cells and LEC/PER object cells in their response to objects. While the role of the PER in object-recognition memory is well-established, the contribution of the hippocampus and LEC to this process remains uncertain[43]. Our results suggested that the enhanced local response to the novel object in dCA1 (Fig. 6) may be due to modified inputs from neurons in the LEC and PER that are specific to object identity[13, 14, 44, 45]. Although further research is required to ascertain whether PER input alone is sufficient for novel object representation in the CA1 region, our findings highlight a potential role for dCA1 in object identity discrimination.

The object-relocation task, essential for studying spatial memory in rodents, prompted our hypothesis of enhanced neural activity in pCA1. However, contrary to our expectations, the ensemble activity in response to object displacement was notably more pronounced in dCA1 (Fig. 5). Moreover, neurons in mCA1 and dCA1 exhibited a much stronger local response to the moved object compared to those in pCA1. This robust local response in the middle-to-distal CA1 regions suggests the influence of additional signals beyond those from MEC object-vector cells and LEC/PER object cells, which respond to objects irrespective of their locations[14, 19, 44, 45, 56]. Two potential sources of these signals include object-trace cells within the LEC, which are theorized to provide dCA1 with supplementary object-place information[15], and dCA1-projecting neurons in the subiculum, which are postulated to modulate place cell activity in response to object displacement[57]. Recently identified subicular corner cells, which generalize

630 their firing to small objects placed in the arena regardless of location[58], may also contribute to
631 this heterogeneity, although whether these cells are indeed the dCA1-projecting neurons
632 remains to be determined.
633
634 While the EC significantly influences the transverse organization of CA1 function,
635 topographical projections from the CA3 and CA2 regions can also play a role. However, unlike
636 the entorhinal inputs, the functional gradients within the CA1 region do not mirror the patterns
637 observed along the CA3-CA2 axis (Fig. 8). Neurons in pCA3 are characterized by sharp and
638 confined place fields, strong rate remapping, and orthogonalized global remapping, whereas
639 neurons in dCA3 and CA2 exhibit reduced spatial modulation and lower sensitivity to
640 environmental changes[31-34]. Interestingly, axons from dCA3 and CA2 preferentially innervate
641 pCA1 neurons, which display enhanced spatial content and pronounced contextual
642 responsiveness. In contrast, pCA3 heavily projects to dCA1, which is characterized by less
643 spatial selectivity and reduced cue-sensitivity[21]. This discrepancy between the functional
644 segregation and projection patterns of CA3-CA2 and CA1 suggests a more complex interaction
645 that warrants further exploration. It is plausible that the less differentiated signals from CA3
646 and CA2 may be overshadowed by the markedly distinct spatial and non-spatial inputs
647 originating from the EC[23].
648
649 This study has two potential limitations. First, CA1 neuronal activity was measured using a
650 hyperdrive with movable tetrodes, which limited our ability to monitor a substantial number of
651 active neurons from various CA1 subregions simultaneously within individual rats. This may
652 have led to inter-animal variability, potentially confounding the interpretation of our results.
653 Second, the complexity in CA1 extends to its radial organization into superficial and deep
654 sublayers, each with distinct characteristics and functions[59]. Our methodology, relying on
655 tetrode recordings, did not enable differentiation between these sublayers. As such, future
656 research endeavors should consider utilizing two-photon calcium imaging and multi-shank
657 probe recordings to conduct a more comprehensive assessment of neural activity across distinct
658 sublayers. The incorporation of these sophisticated methodologies may yield deeper insights
659 into the role that laminar variations play in the observed heterogeneity of functions along the

CA1 proximodistal axis.

To conclude, the present study identified three distinct patterns of cue representation along the proximodistal axis of the CA1 region. These findings necessitate further investigation into the causal dynamics linking selective inputs from specific upstream neuronal populations with the downstream representation of diverse information. Future theoretical and experimental endeavors should focus on uncovering the precise mechanisms that govern these interactions, which are crucial for elucidating the neural basis of spatial navigation, episodic memory, and broader cognitive functions of the hippocampus.

Methods

Subjects

The experiments were conducted at the Kunming Institute of Zoology, Chinese Academy of Sciences (Kunming, China) in compliance with the guidelines for the care and use of laboratory animals. The study received approval from the Institutional Animal Care and Use Committee of the Kunming Institute of Zoology (KIZ-IACUC-RE-2021-06-019). Data were collected from 20 male Long-Evans rats (3–4 months old, 500–600 g at the time of implantation). Five rats (IDs: 17899, 18547, 18548, 18549, and 19326) from a previous study [32] contributed proximal-to-middle CA1 data. The remaining 15 rats (IDs: R0087, R0088, R0089, R0092, R0172, R0175, R0388, R0389, R0390, R0391, R0621, R0769, R0836, R1026, and R1028) were implanted with a multi-tetrode "hyperdrive" targeting the right hippocampus. The animals were maintained on a reversed 12-hour light/dark cycle (lights off from 9.00 am to 9.00 pm) under standard laboratory conditions (temperature: 20–23 °C, relative humidity: 40%–60%). Following surgery, the rats were housed individually, and experimental procedures were conducted during the dark phase. During the experimental period, the animals were mildly food restricted to maintain their weight at 85%–90% of free-feeding body weight.

Electrode preparation

The multi-tetrode "hyperdrive", consisting of 18 independently movable tetrodes made of 17

μm polyimide-coated platinum-iridium (90%–10%) wire (California Fine Wires, USA), was prepared as described previously[60]. The electrode tips were plated to reduce impedance to 150–250 kΩ at 1 kHz (Biomega, Bio-Signal Technologies, China) and sterilized with ethylene oxide (Sanqiang Medical, China) within 48 hours before implantation.

Surgery

Rats were anesthetized with isoflurane (air flow: 0.8–1.0 L/min, 0.5–3% isoflurane vol/vol mixed with oxygen), with the concentration adjusted based on physiological monitoring (RWD Life Science, China). Upon induction of anesthesia, Metacam (2 mg/mL, 1 mg/kg body weight), Baytril (50 mg/mL, 5 mg/kg), and atropine (0.5 mg/mL, 0.1 mg/kg) were administered subcutaneously. The animal's head was then fixed in a stereotaxic frame (RWD Life Science, China). Local anesthetic (2% lidocaine, 200 μL) was applied under the skin before making the incision. The skull and dura were removed, followed by immediate hyperdrive implantation. Tetrodes were inserted at the cortical surface above the right hippocampus (anteroposterior (AP) from 3.2 to 5.6 mm, mediolateral (ML) from 1.0 to 4.5 mm relative to bregma). The hyperdrive was secured to the skull with jewelers' screws and dental cement. Grounding was achieved by connecting two screws above the cerebellum to the hyperdrive ground, while two reference tetrodes were positioned in an inactive area of the cortex for differential recording.

Electrophysiological recordings

For the first 3–4 weeks post-surgery, the tetrodes were advanced daily until they reached the dorsal CA1 pyramidal cell layer, characterized by large-amplitude theta-modulated complex-spike activity. On the recording day, the electrodes were kept stationary to ensure stable recordings. Broadband neural signals were captured from the hyperdrive using a multichannel data acquisition system (Zeus, Bio-Signal Technologies, China). Unit activity was amplified (× 192) and band-pass filtered (300 to 7 500 Hz). Spike waveforms that exceeded the −50 μV threshold were time-stamped and digitized at 30 kHz for 1 ms. Local field potential (LFP) signals, one per tetrode, were recorded in the 0.3–300 Hz frequency band at a sampling rate of 1 000 Hz. The animal's position was monitored in real-time by tracking light-emitting diodes (LEDs) on the headstage at 50 Hz using a Cyclops video tracking system (Bio-Signal

Technologies, China).

Behavioral paradigms

Each task consisted of four 10-minute exploration trials within the recording box, interspersed with five 5-minute rest periods in a flowerpot placed on a pedestal outside the box. The exploration trials were designed in an A-B-B-A configuration, where A and B represented distinct test conditions. To encourage exploration, cookie crumbs were randomly scattered throughout the recording box. One week after surgery, the mildly food-restricted rats were trained daily in the color-reversal task in two separate rooms until they could traverse the entire arena within 10 minutes in all trials. Once the tetrodes reached the CA1 cell layer, the animal underwent sequential testing and recording in the color-reversal, two-room, and three object-related tasks.

Test environments

Recording boxes (100 cm × 100 cm) consisted of a metal frame and four individually exchangeable plastic walls (black on one side, white on the other; 100 cm × 50 cm). Cue cards (white cue card for black walls and vice versa; 50 cm × 30 cm) were placed at the center of one wall. Distal background cues were obscured by curtains encircling the recording box (120 cm × 120 cm) for the color-reversal and object-related tasks but not for the two-room task. The pedestal with the flowerpot was positioned between the test box and experimenter, outside the curtains. The recording rooms for the two-room task were similar in size but featured different spatial arrangements.

Color-reversal task

As detailed previously, this task was designed to elicit rate remapping in the hippocampus[32, 37, 38]. 15 rats were trained/tested in the recording box at a fixed location over four trials daily, with trials 1 and 4 conducted with black walls and trials 2 and 3 conducted with white walls. The floor of the recording box was cleaned with 75% ethanol after each trial.

Two-room task

This task was designed to evoke global remapping in the hippocampus[32, 37]. 15 rats were tested in similar recording boxes with black walls located at fixed locations in two separate recording rooms, with trials 1 and 4 conducted in room A and trials 2 and 3 conducted in room B. The floor of the recording box was cleaned with 75% ethanol after each trial.

Tasks with objects

The object-related tasks were designed to induce local firing changes in the hippocampus[39, 40]. 14 rats (excluding R0087) were sequentially tested in the object-placement, object-relocation, and novel-object tasks following the two-room task. For each task, the floor of the recording box and the objects were thoroughly cleaned with 75% ethanol before each trial.

Object-placement task: Animals were tested in the black recording box at a fixed location over four trials, with two identical familiar objects (glass bottles filled with white stones) placed in quadrants 3 and 4 of the box for trials 2 and 3.

Object-relocation task: Animals were tested in the black recording box containing two familiar objects over four trials, with the object in quadrant 4 relocated to quadrant 1 for trials 2 and 3.

Novel-object task: Animals were tested in the black recording box containing two objects over four trials, with the familiar object in quadrant 4 replaced by a novel object in trials 2 and 3.

Occupation time and discrimination index

Occupation time (OT) and discrimination index (DI) were employed to quantify preference for objects in the object-placement task and for relocated/novel objects in the object-relocation and novel-object tasks. OT was defined as the proportion of time spent around the objects relative to the total time spent in the recording box, and DI was calculated as:

$$DI = \frac{T_r - T_u}{T_r + T_u};$$

where T_r is the time spent around the relocated/replaced object and T_u is the time spent around the unchanged object. A higher DI value indicates a greater preference for the relocated/novel

object.

Histology and recording sites

Following the completion of electrophysiological recordings, the electrodes were maintained in their positions. The rats were subsequently euthanized and perfused with formalin for brain extraction. Frozen brain sections (40 μm thick) were cut on a cryostat (KEDEE, KD-2950, China), and stained using cresyl-violet (Sigma Aldrich, USA, CAS: 10510-54-0, Cat# C5042-10G). the Nissl-stained brain sections were imaged using a bright-field microscope (2×/0.06, 4 ×/0.13 NA objectives, COIC, UB103i, China), with UOPView software (v2.0). The location of each tetrode tip was then identified and recorded. Hippocampal subregions were delineated based on established criteria[21, 30]. ImageJ (v1.52a) was used to estimate the normalized position along the proximodistal axis of the CA1 region for each recording site. Hand-drawn lines tracing the CA1 pyramidal cell layer were extended from the CA2/CA1 border to the CA1/subiculum border, passing through the recording site on each section. The distance from the CA2/CA1 border to the recording site was measured and normalized by the total length of the CA1 region on the same section. Based on these normalized positions, recording sites were categorized into proximal (pCA1, 0–0.33), middle (mCA1, 0.33–0.67), and distal (dCA1, 0.67–1) subregions.

LFP power

LFP signals were collected within a 15 cm radius around each object during trials 1 and 2, then extracted and concatenated for analysis. Using the Chronux Toolbox in Matlab (v2.12, http://chronux.org/), absolute power spectra were estimate for consecutive 5-second time windows of the LFP, spanning frequencies from 0 to 100 Hz[61]. The time-bandwidth product (TW) was set to 3, with the number of tapers (K) set to 5. The normalized change in LFP power at each frequency (1 Hz bins) surrounding each object was calculated using the following formula:

$$LFP\ power\ change = \frac{P_2 - P_1}{P_2 + P_1};$$

where P_2 and P_1 represent the absolute LFP power at a specific frequency near the object in

807 trials 2 and 1, respectively. Experiments with subpar recording quality were excluded from
808 further analysis.
809
810 **Spike sorting and cell classification**
811 Spike sorting was manually performed using the MClust graphical cluster-cutting tool in
812 Matlab (v4.4, A.D. Redish). The process involved the analysis of two-dimensional projections
813 of the multidimensional parameter space, consisting of waveform amplitudes, waveform
814 energies, and waveform peak-valley differences. Waveform and autocorrelation functions were
815 also employed as tools for separation and classification. Clustering was applied on the entire
816 dataset of each experiment, with the spikes subsequently divided into four exploration trials.
817
818 Putative excitatory cells were distinguished from putative interneurons and bypassing axons
819 based on spike width (peak-to-trough waveform durations greater than 250 μs), average rate
820 (less than 5 Hz), and occasional presence of bursts. Only cells classified as putative excitatory
821 neurons were included in subsequent analyses. Cells recorded repeatedly in the same task were
822 excluded from analyses.
823
824 **Rate maps and place fields**
825 Position estimates were derived from tracking the LEDs on the headstage connected to the
826 hyperdrive. Data were filtered to include only epochs with instantaneous running speeds
827 between 2.5 and 100 cm/s. The mean firing rate for each cell was calculated by summing the
828 total number of spikes and dividing it by the time spent in that trial. Place field analyses were
829 conducted exclusively for cells with a mean firing rate of 0.10 Hz or higher, defined as active
830 cells. Spatial firing rate distributions (place fields) for each well-isolated neuron were generated
831 by summing the spikes within specific location bins (5 cm × 5 cm), dividing by the duration of
832 time spent by the rat in that location, and applying Gaussian smoothing centered on each bin,
833 as described previously[32]. A place field was defined as a contiguous region of at least 225 cm^2
834 (nine or more 5 × 5 cm bins) where the firing rate exceeded 20% of the peak rate and the peak
835 firing rate of the area was 1 Hz or greater. The number of non-overlapping place fields was
836 estimated for each cell.

Theta modulation and phase locking

The theta modulation index (TMI) was computed to assess the temporal modulation of firing within the theta frequency range (7–10 Hz) of each cell, as described previously[62]. A temporal autocorrelogram was constructed by tallying the occurrences of spikes within each 5-ms bin over a range of 0 to 500 ms from a reference spike at time 0, then dividing by the total trial length to determine the rate of occurrence for each bin. The TMI was calculated as:

$$TMI = \frac{P-T}{P+T};$$

where P and T represent the theta modulation peak (mean of bins 100–140 ms) and trough (mean of time bins 50–70 ms), respectively.

Theta phase locking was quantified to measure the coupling of CA1 cells to hippocampal theta oscillations. LFP recordings were bandpass-filtered within the theta range (7–10 Hz), and theta phases for each time point were estimated using the Hilbert transform function from the Signal Processing Toolbox in Matlab (MathWorks, USA). Theta phases for CA1 place cell spikes were collected and sorted into 10° bins. Mean vector length (MVL) was calculated using the Circular Statistics Toolbox in Matlab (v1.21, P. Berens):

$$MVL = \left|\frac{1}{n}\sum_i (a_i\, cos(\theta_i) + j a_i\, sin(\theta_i))\right|;$$

where j is the imaginary number, n is the number of circular bins ($n = 36$), θ_i and a_i are the theta phase and response for the i-th bin, respectively.

Spatial information, coherence, and stability

The spatial information rate in bits per second (SI_r) and spatial information content in bits per spike (SI_c) were calculated as described in previous research[63]:

$$SI_r = \sum_i p_{i\lambda_i} \log_2 \frac{\lambda_i}{\lambda};\ SI_c = \sum_i p_i \frac{\lambda_i}{\lambda} \log_2 \frac{\lambda_i}{\lambda};$$

where λ_i is the mean firing rate of a unit in the i-th bin, λ is the overall mean firing rate, and p_i is the probability of the animal being in the i-th bin (occupancy in the i-th bin / total recording time).

Spatial coherence was estimated as the first-order spatial autocorrelation of the unsmoothed place field map, i.e., mean correlation between the firing rate of each bin and average firing rate in the eight adjacent bins.

Spatial stability was determined by comparing the firing pattern in the first half of each trial to that in the second half. The rate map for each half was smoothed and binned into 5 cm × 5 cm matrices, and the firing rates in the bins of the two half-trial maps were correlated for each trial.

Spatial correlation (SC)

Firing patterns were compared across trials using a SC procedure. Each map was smoothed and binned into 5 × 5 cm matrices, and the firing rates in the pixels of the two maps were correlated for each cell. SC between two inactive trials (firing rates below 0.1 Hz) was excluded to avoid artifacts. For the two-room task, rate maps were rotated in 90° steps to identify the maximum SC score when compared across rooms. For the color-reversal and two-room tasks, firing patterns were compared between trials 1 and 3 and between trials 2 and 4 for different conditions to minimize the effect of elapsed time, while trials 1 and 4 and trials 2 and 3 were compared for matching conditions. For the object-related tasks, firing patterns were compared between trials 1 and 2 for different conditions, and between trials 2 and 3 for matching conditions to avoid the effect of hysteresis in trial 4.

Rate difference (RD) and rate difference by field (RD_f)

The change in overall firing rate across trials was calculated as RD:

$$RD = \left|\frac{FR_1 - FR_2}{FR_1 + FR_2}\right|;$$

where FR_1 is the mean firing rate of a cell in one trial and FR_2 is the mean firing rate of the same cell in a second trial, with RD = 1 indicating that the cell was active in one trial only and RD = 0 indicating that the firing rates in the two trials were the same.

The RD_f was computed to mitigate the neutralization effect across individual place fields from the same cell:

$$RD_f = \sum_i w_i RD_i \;;$$

where RD_i is the rate difference of the i-th place field and w_i is the weight of the i-th place field estimated from its firing rate. RD_f was not computed when changes in firing location occurred.

Population vector correlation (PVC)

Rate vectors were constructed for the entire population of cells recorded under each condition, including those with firing rates below 0.1 Hz and spatial information content below 0.9586 bits/spike. This process involved arranging all rate maps for all cells in an x-y-z stack, with x and y denoting the two spatial dimensions (20 × 20 bins) and z representing the cell-identity index[37]. For the two-room task, rate maps were rotated analogously to the SC analyses performed for each cell. The distribution of bin rates along the z axis for a specific x-y location represented the composite population vector for that location. Population vectors from corresponding positions were then correlated across pairs of trials.

Shuffling

Shuffling of spatial information was conducted on a cell-by-cell basis, as described previously[30]. Each CA1 cell recorded from the color-reversal task underwent 100 permutations. In each permutation, the entire sequence of spikes fired by the cell was time-shifted along the animal's path by a random interval ranging from 20 seconds to the total trial length minus 20 seconds. The end of the trial was wrapped back to the beginning to allow for circular displacements. A rate map was generated for each permutation, and the distribution of spatial information values across all permutations for all CA1 cells was determined. A putative excitatory neuron was classified as a place cell if its spatial information content exceeded the 95th percentile of the shuffled distribution (0.9586 bits/spike).

For each CA1 band, a control distribution for SC analyses was established using a random permutation procedure. This procedure involved all active maps (mean firing rates higher than 0.10 Hz) from all cells recorded within that band[32]. For each permutation, two distinct active maps from different cells were randomly selected and correlated in 90° rotation steps to achieve the highest correlation score. In total, 10 000 permutations were performed for each CA1 band.

This method preserved the rate maps within each band while eliminating connections between maps. The distribution of random correlations from all 10 000 permutations was then calculated, and the 95th percentile was determined.

Bayesian decoding

A Bayesian decoding algorithm was employed to convert ensemble spiking activity into positional information for each experiment. The decoding process used a 2 000 ms sliding time window, advancing by 200 ms with each step. The probability of a rat being at position x, given the number of spikes n from each unit recorded within the time window, was estimated using Bayes' rule[64]:

$$P(x \mid n) = \frac{P(n|x)P(x)}{P(n)};$$

The probabilistic likelihood $P(n|x)$ was calculated using the probability mass function of the Poisson distribution to determine the likelihood of observing a specific number of spikes given the activity pattern of a neuron:

$$P(n \mid x) = \frac{e^{-\lambda}\lambda^{n}}{n!};$$

where λ is the expected number of spikes based on the tuning curve and n is the actual observed number of spikes within the given time window. The prior probability of position $P(x)$ was set to the frequency of the animal's presence in each state within the training data. The normalizing constant $P(n)$ ensured that the posterior probability $P(x|n)$ summed to 1. For visualization and maximum decoding performance estimation, only experiments with over 30 simultaneously recorded place cells in both CA1 bands were considered. Downsampling was applied to equalize cell numbers and repeated three times to determine the mean decoding accuracy value. For position decoding, 90% of the data from the four trials served as the training set, while the remaining 10% was used as the test set. This cross-validation procedure was repeated 10 times (10-fold validation). For context decoding, data from trials 2 and 3 formed the training set, with 90% of trial 1 data serving as the test set. This procedure was also repeated 10 times. Decoding accuracy was expressed as:

$$R^2 = 1 - \frac{\Sigma_i(\hat{y}_i - y_i)^2}{\Sigma_i(y_i - \bar{y})^2};$$

Where $\hat{y}_i$ and y_i are the predicted and true positions of the i-th time bin, respectively, and $\bar{y}$ is

the mean position value.

Fitting

The EzyFit Toolbox in Matlab (v2.44) was used to compute curve fitting for the average data obtained from the tetrodes. The explained variance was calculated as:

$$R^2 = \frac{\Sigma_i(\hat{y}_i - \bar{y})^2}{\Sigma_i(y_i - \bar{y})^2};$$

where $\hat{y}_i$ is the predicted value based on the curve fitting and normalized position of each tetrode, y_i is the average tetrode data, and $\bar{y}$ is the mean value across all tetrodes.

Statistical procedures

Results are presented as medians and interquartile ranges (IQR) due to the non-normal distribution of most data. The Kruskal-Wallis test was used to compare the firing properties of cells across CA1 bands. The Mann-Whitney U test was employed to compare two groups of unrelated measures, while the Wilcoxon signed-rank test and paired *t*-test were employed to compare two related measures. One-way repeated-measures analysis of variance (ANOVA) was applied to analyze running speed across trials. Regional differences in remapping between two conditions were assessed using two-way repeated-measures ANOVA with a 3 × 2 factor design, considering condition pairs (matching or different) as within-subject factors and CA1 bands as between-subjects factors. Two-way repeated-measures ANOVA was also used when comparing data across recording experiments. The Pearson chi-square test and Fisher's exact test were applied to compare frequency distributions across groups, and Pearson correlation was calculated to measure the linear correlation between two variables. The binomial test was applied to determine whether the observed frequency differed from the expected frequency. Holm-Bonferroni *post-hoc* tests were used to identify significant differences between pairs, while the Benjamini and Hochberg method was applied to correct for the false discovery rate (FDR) in multiple hypothesis testing. The significance level was set at $P < 0.05$ for two-tailed tests. All statistical analyses were conducted using SPSS v25 (IBM, USA).

Editing

Kimi AI was used exclusively for language refinement. The authors reviewed and edited the output as needed and take full responsibility for the content of the publication.

Data availability

The data supporting the findings of this study are available from the corresponding author upon reasonable request.

References

1. Sugar, J. & Moser, M.B. Episodic memory: Neuronal codes for what, where, and when. *Hippocampus* **29**, 1190-1205 (2019).
2. Colgin, L.L., Moser, E.I. & Moser, M.B. Understanding memory through hippocampal remapping. *Trends Neurosci* **31**, 469-477 (2008).
3. Latuske, P., Kornienko, O., Kohler, L. & Allen, K. Hippocampal Remapping and Its Entorhinal Origin. *Front Behav Neurosci* **11**, 253 (2017).
4. Canto, C.B., Wouterlood, F.G. & Witter, M.P. What does the anatomical organization of the entorhinal cortex tell us? *Neural Plast* **2008**, 381243 (2008).
5. Hafting, T., Fyhn, M., Molden, S., Moser, M.B. & Moser, E.I. Microstructure of a spatial map in the entorhinal cortex. *Nature* **436**, 801-806 (2005).
6. Fyhn, M., Molden, S., Witter, M.P., Moser, E.I. & Moser, M.B. Spatial representation in the entorhinal cortex. *Science* **305**, 1258-1264 (2004).
7. Sargolini, F*., et al.* Conjunctive representation of position, direction, and velocity in entorhinal cortex. *Science* **312**, 758-762 (2006).
8. Solstad, T., Boccara, C.N., Kropff, E., Moser, M.B. & Moser, E.I. Representation of geometric borders in the entorhinal cortex. *Science* **322**, 1865-1868 (2008).
9. Kropff, E., Carmichael, J.E., Moser, M.B. & Moser, E.I. Speed cells in the medial entorhinal cortex. *Nature* **523**, 419-424 (2015).
10. Tukker, J.J*., et al.* Microcircuits for spatial coding in the medial entorhinal cortex. *Physiol Rev* **102**, 653-688 (2022).
11. Long, J.L. & Lu, L. Dynamic coding in the hippocampus during navigation. *Zool Res* **43**,

1023-1025 (2022).

12. Hargreaves, E.L., Rao, G., Lee, I. & Knierim, J.J. Major dissociation between medial and lateral entorhinal input to dorsal hippocampus. *Science* **308**, 1792-1794 (2005).

13. Huang, X.*, et al.* Distinct spatial maps and multiple object codes in the lateral entorhinal cortex. *Neuron* **111**, 3068-3083 e3067 (2023).

14. Deshmukh, S.S. & Knierim, J.J. Representation of non-spatial and spatial information in the lateral entorhinal cortex. *Front Behav Neurosci* **5**, 69 (2011).

15. Tsao, A., Moser, M.B. & Moser, E.I. Traces of experience in the lateral entorhinal cortex. *Curr Biol* **23**, 399-405 (2013).

16. Igarashi, K.M., Lu, L., Colgin, L.L., Moser, M.B. & Moser, E.I. Coordination of entorhinal-hippocampal ensemble activity during associative learning. *Nature* **510**, 143-147 (2014).

17. Leitner, F.C.*, et al.* Spatially segregated feedforward and feedback neurons support differential odor processing in the lateral entorhinal cortex. *Nat Neurosci* **19**, 935-944 (2016).

18. Tsao, A.*, et al.* Integrating time from experience in the lateral entorhinal cortex. *Nature* **561**, 57-62 (2018).

19. Wang, C.*, et al.* Egocentric coding of external items in the lateral entorhinal cortex. *Science* **362**, 945-949 (2018).

20. Knierim, J.J., Neunuebel, J.P. & Deshmukh, S.S. Functional correlates of the lateral and medial entorhinal cortex: objects, path integration and local-global reference frames. *Philos Trans R Soc Lond B Biol Sci* **369**, 20130369 (2014).

21. Cappaert, N.L., van Strien, N.M. & Witter, M.P. Hippocampal Formation. in *The Rat Nervous System* (ed. G. Paxinos) 511-573 (Academic Press,, 2015).

22. Nilssen, E.S., Doan, T.P., Nigro, M.J., Ohara, S. & Witter, M.P. Neurons and networks in the entorhinal cortex: A reappraisal of the lateral and medial entorhinal subdivisions mediating parallel cortical pathways. *Hippocampus* **29**, 1238-1254 (2019).

23. Masurkar, A.V.*, et al.* Medial and lateral entorhinal cortex differentially excite deep versus superficial CA1 pyramidal neurons. *Cell Rep* **18**, 148-160 (2017).

24. Nakamura, N.H., Flasbeck, V., Maingret, N., Kitsukawa, T. & Sauvage, M.M. Proximodistal segregation of nonspatial information in CA3: preferential recruitment of a

1042 proximal CA3-distal CA1 network in nonspatial recognition memory. *J Neurosci* **33**, 11506-
1043 11514 (2013).
1044 25. Beer, Z.*, et al.* The memory for time and space differentially engages the proximal and
1045 distal parts of the hippocampal subfields CA1 and CA3. *PLoS Biol* **16**, e2006100 (2018).
1046 26. Flasbeck, V., Atucha, E., Nakamura, N.H., Yoshida, M. & Sauvage, M.M. Spatial
1047 information is preferentially processed by the distal part of CA3: Implication for memory
1048 retrieval. *Behav Brain Res* **354**, 31-38 (2018).
1049 27. Ito, H.T. & Schuman, E.M. Functional division of hippocampal area CA1 via modulatory
1050 gating of entorhinal cortical inputs. *Hippocampus* **22**, 372-387 (2012).
1051 28. Nakazawa, Y., Pevzner, A., Tanaka, K.Z. & Wiltgen, B.J. Memory retrieval along the
1052 proximodistal axis of CA1. *Hippocampus* **26**, 1140-1148 (2016).
1053 29. Hartzell, A.L.*, et al.* Transcription of the immediate-early gene Arc in CA1 of the
1054 hippocampus reveals activity differences along the proximodistal axis that are attenuated by
1055 advanced age. *J Neurosci* **33**, 3424-3433 (2013).
1056 30. Henriksen, E.J.*, et al.* Spatial representation along the proximodistal axis of CA1. *Neuron*
1057 **68**, 127-137 (2010).
1058 31. Lee, H., Wang, C., Deshmukh, S.S. & Knierim, J.J. Neural population evidence of
1059 functional heterogeneity along the CA3 transverse axis: pattern completion versus pattern
1060 separation. *Neuron* **87**, 1093-1105 (2015).
1061 32. Lu, L., Igarashi, K.M., Witter, M.P., Moser, E.I. & Moser, M.B. Topography of place maps
1062 along the CA3-to-CA2 axis of the hippocampus. *Neuron* **87**, 1078-1092 (2015).
1063 33. Oliva, A., Fernandez-Ruiz, A., Buzsaki, G. & Berenyi, A. Spatial coding and physiological
1064 properties of hippocampal neurons in the Cornu Ammonis subregions. *Hippocampus* **26**, 1593-
1065 1607 (2016).
1066 34. Deshmukh, S.S. Distal CA1 Maintains a More Coherent Spatial Representation than
1067 Proximal CA1 When Local and Global Cues Conflict. *J Neurosci* **41**, 9767-9781 (2021).
1068 35. Li, Y.*, et al.* A distinct entorhinal cortex to hippocampal CA1 direct circuit for olfactory
1069 associative learning. *Nat Neurosci* **20**, 559-570 (2017).
1070 36. Leutgeb, S., Leutgeb, J.K., Treves, A., Moser, M.B. & Moser, E.I. Distinct ensemble codes
1071 in hippocampal areas CA3 and CA1. *Science* **305**, 1295-1298 (2004).

37. Leutgeb, S., *et al.* Independent codes for spatial and episodic memory in hippocampal neuronal ensembles. *Science* **309**, 619-623 (2005).

38. Lu, L., *et al.* Impaired hippocampal rate coding after lesions of the lateral entorhinal cortex. *Nat Neurosci* **16**, 1085-1093 (2013).

39. Vandrey, B., Duncan, S. & Ainge, J.A. Object and object-memory representations across the proximodistal axis of CA1. *Hippocampus* **31**, 881-896 (2021).

40. Nagelhus, A., Andersson, S.O., Cogno, S.G., Moser, E.I. & Moser, M.B. Object-centered population coding in CA1 of the hippocampus. *Neuron* **111**, 2091-2104 e2014 (2023).

41. Deshmukh, S.S. & Knierim, J.J. Influence of local objects on hippocampal representations: Landmark vectors and memory. *Hippocampus* **23**, 253-267 (2013).

42. Burke, S.N., *et al.* The influence of objects on place field expression and size in distal hippocampal CA1. *Hippocampus* **21**, 783-801 (2011).

43. Aggleton, J.P. & Nelson, A.J.D. Distributed interactive brain circuits for object-in-place memory: A place for time? *Brain Neurosci Adv* **4**, 2398212820933471 (2020).

44. Burke, S.N., *et al.* Representation of three-dimensional objects by the rat perirhinal cortex. *Hippocampus* **22**, 2032-2044 (2012).

45. Deshmukh, S.S., Johnson, J.L. & Knierim, J.J. Perirhinal cortex represents nonspatial, but not spatial, information in rats foraging in the presence of objects: comparison with lateral entorhinal cortex. *Hippocampus* **22**, 2045-2058 (2012).

46. Fyhn, M., Hafting, T., Treves, A., Moser, M.B. & Moser, E.I. Hippocampal remapping and grid realignment in entorhinal cortex. *Nature* **446**, 190-194 (2007).

47. Renno-Costa, C., Lisman, J.E. & Verschure, P.F. The mechanism of rate remapping in the dentate gyrus. *Neuron* **68**, 1051-1058 (2010).

48. Diehl, G.W., Hon, O.J., Leutgeb, S. & Leutgeb, J.K. Grid and Nongrid Cells in Medial Entorhinal Cortex Represent Spatial Location and Environmental Features with Complementary Coding Schemes. *Neuron* **94**, 83-92 e86 (2017).

49. Ismakov, R., Barak, O., Jeffery, K. & Derdikman, D. Grid Cells Encode Local Positional Information. *Curr Biol* **27**, 2337-2343 e2333 (2017).

50. Marozzi, E., Ginzberg, L.L., Alenda, A. & Jeffery, K.J. Purely Translational Realignment in Grid Cell Firing Patterns Following Nonmetric Context Change. *Cereb Cortex* **25**, 4619-

4627 (2015).

51. Miao, C., *et al.* Hippocampal Remapping after Partial Inactivation of the Medial Entorhinal Cortex. *Neuron* **88**, 590-603 (2015).

52. Rueckemann, J.W., *et al.* Transient optogenetic inactivation of the medial entorhinal cortex biases the active population of hippocampal neurons. *Hippocampus* **26**, 246-260 (2016).

53. Kanter, B.R., *et al.* A Novel Mechanism for the Grid-to-Place Cell Transformation Revealed by Transgenic Depolarization of Medial Entorhinal Cortex Layer II. *Neuron* **93**, 1480-1492 e1486 (2017).

54. Masurkar, A.V., *et al.* Postsynaptic integrative properties of dorsal CA1 pyramidal neuron subpopulations. *J Neurophysiol* **123**, 980-992 (2020).

55. Zeng, Y.F., *et al.* Conjunctive encoding of exploratory intentions and spatial information in the hippocampus. *Nature Communications* **15** (2024).

56. Hoydal, O.A., Skytoen, E.R., Andersson, S.O., Moser, M.B. & Moser, E.I. Object-vector coding in the medial entorhinal cortex. *Nature* **568**, 400-404 (2019).

57. Sun, Y., *et al.* CA1-projecting subiculum neurons facilitate object-place learning. *Nat Neurosci* **22**, 1857-1870 (2019).

58. Sun, Y., Nitz, D.A., Xu, X. & Giocomo, L.M. Subicular neurons encode concave and convex geometries. *Nature* **627**, 821-829 (2024).

59. Soltesz, I. & Losonczy, A. CA1 pyramidal cell diversity enabling parallel information processing in the hippocampus. *Nat Neurosci* **21**, 484-493 (2018).

60. Lu, L., Popeney, B., Dickman, J.D. & Angelaki, D.E. Construction of an Improved Multi-Tetrode Hyperdrive for Large-Scale Neural Recording in Behaving Rats. *J Vis Exp* (2018).

61. Bokil, H., Andrews, P., Kulkarni, J.E., Mehta, S. & Mitra, P.P. Chronux: a platform for analyzing neural signals. *J Neurosci Methods* **192**, 146-151 (2010).

62. Cacucci, F., Lever, C., Wills, T.J., Burgess, N. & O'Keefe, J. Theta-modulated place-by-direction cells in the hippocampal formation in the rat. *J Neurosci* **24**, 8265-8277 (2004).

63. Skaggs, W.E., McNaughton, B.L., Wilson, M.A. & Barnes, C.A. Theta phase precession in hippocampal neuronal populations and the compression of temporal sequences. *Hippocampus* **6**, 149-172 (1996).

64. Glaser, J.I., *et al.* Machine Learning for Neural Decoding. *eNeuro* **7** (2020).

Acknowledgments

The authors express gratitude to Yi-Qing Hui, Yi-Fan Ye, Chang-Lin Shen, and Yi-Ling Shi for their technical assistance in animal care, single-unit isolation and Matlab coding. They also thank Edvard Moser and May-Britt Moser for providing the Behavioral Neurology Toolbox and data from five animals, and Cheng Wang, Xin-Jian Li, Dun Mao, Hai-Bing Xu, and Yong-Gang Yao for their valuable suggestions on the manuscript.

Author Contributions

LL designed the experiments and analyses; YLD, SYH, XFG, JLL, CD, CJL, RZ, and XC performed the experiments; YLD, SYH, and LL conducted the analyses; YMS carried out the Bayesian decoding. YLD, XC, and LL wrote the manuscript. All authors contributed to discussion and interpretation of the results.

Funding

This research was supported by the Science and Technology Innovation (STI) 2030-Major Projects (2022ZD0205000 to LL), National Natural Science Foundation of China (31970963 to LL), Yunnan Revitalization Talent Support Program (Yunling Scholar Project to LL), Yunnan Province (202305AH340006 to LL), and Yunnan Fundamental Research Projects (202101AT070289 to XC).

Conflict of interest statement

The authors declare no competing financial interests.

Code accessibility

All custom-written codes used in the analyses are available upon request.

Supplementary material

Supplementary material is accessible in the online version of this paper.

Figure legends

Fig. 1: Recording sites and graded spatial modulation along CA1 transverse axis.

a, Left: recording region within dorsal hippocampus, shown in red. Right: distribution of recording sites along proximodistal axis of CA1. Red dots represent location of tetrode tips. Solid lines indicate borders between hippocampal regions; dashed lines separate proximal, middle, and distal bands of CA1. Numbers indicate normalized positions in CA1 along the transverse axis. FC: fasciola cinereum; SUB: subiculum. For a detailed view of recording sites per animal, refer to Supplementary Fig. 1.

b, Representative firing rate distribution maps (rate maps) from simultaneously recorded CA1 neurons in two separate experiments. Top: rate maps of pCA1 and mCA1 place cells recorded from rat R0388. Gray lines indicate trajectories of animal in each trial. Rate maps of each cell are arranged in rows, with cell ID and peak firing rate for each trial indicated. Color is scaled to maximum peak rate of four trials. B, black; W, white version of the same box. Bottom: rate maps of mCA1 and dCA1 place cells recorded from rat R0175. Note, confined firing fields in more proximally located place cells and profound rate remapping in pCA1.

c–**h**, Violin plots displaying distributions of peak rate (**c**), number of place fields (**d**), theta modulation index (**e**), spatial information content (**f**), spatial coherence (**g**), and spatial stability (**h**) of place cells recorded in each CA1 band. Horizontal line indicates median, and thick vertical bar indicates interquartile range (IQR, 25%–75% percentile) of each subregion. *: $P < 0.05$; **: $P < 0.01$; ***: $P < 0.001$.

i–**n**, Scatter plots showing correlations between normalized recording position and peak rate (**i**), place field number (**j**), theta modulation (**k**), spatial information (**l**), coherence (**m**), and stability (**n**). Each cross represents average data of a single tetrode. Blue curve, linear regression; red curve, quadratic polynomial regression. Explained variances (R^2) are indicated with the same color code, with Pearson correlation coefficients and *P* values provided. pro., proximal end; dis., distal end.

Fig. 2: Reverse J-shaped rate remapping to reversed wall color across CA1 subdivisions.

a, Left: distributions of SC in CA1 subregions between matching (Same, mean of 2-3 trial pair and 1-4 trial pair) and color reversed (B vs W, mean of 1-3 trial pair and 2-4 trial pair) conditions in the color-reversal task. Horizontal line indicates median, and thick vertical bar indicates IQR of each subregion. Right: box plots representing changes in SC between condition pairs, with outliers omitted. Place cells in mCA1 exhibited least activity change. *: $P < 0.05$; ***: $P < 0.001$.

b, Changes in SC between condition pairs as a function of tetrode position. Each cross corresponds to average data of a single tetrode. Blue curve, linear regression; red curve, quadratic polynomial regression. Explained variances (R^2) are indicated with the same color code. pro., proximal end; dis., distal end. p, proximal half; d, distal half.

c, Similar to **a** but showing changes in RD across CA1 subdivisions. ***: $P < 0.001$.

d, Similar to **b** but showing correlations between tetrode position and changes in RD between condition pairs.

e, Similar to **a** but showing changes in PVC across CA1 bands. ***: $P < 0.001$.

f, Heatmaps showing PVC of all putative pyramidal neurons recorded from each CA1 subregion between color conditions (top two rows), and changes in PVC between condition pairs (bottom row) in the color-reversal task. Heatmap bins correspond to spatial bins in rate maps. Color scales are indicated on the right of each row. Note, mCA1 exhibited the lowest activity changes. Reduction in PVC is stronger for spatial bins away from arena walls, where the color was manipulated.

Fig 3: Graded global remapping along proximodistal axis in CA1.

a, Simultaneously recorded CA1 neurons in two rats exhibiting global remapping in the two-room task. Left: rate maps of pCA1 and mCA1 place cells recorded from rat R0172. Gray lines indicate trajectories of animal in each trial. Rate maps of each cell are arranged in rows, with cell ID and peak firing rate for each trial indicated. Color is scaled to maximum peak rate of four trials. A, Room A; B, Room B. Right: rate maps of mCA1 and dCA1 place cells recorded from rat R0175. Note, redistribution of firing locations between different rooms.

b, Left: distribution of SC in CA1 subdivisions in the same room (Same, mean of 2-3 trial pair

1219 and 1-4 trial pair) and in different rooms (Room A vs B, mean of 1-3 trial pair and 2-4 trial pair)
1220 in the two-room task. Horizontal line indicates median, and thick vertical bar indicates IQR of
1221 each subregion. Right: change in SC between condition pairs, with outliers omitted. Place cells
1222 in pCA1 exhibited the strongest activity change. ***: $P < 0.001$.
1223 **c**, Correlation between tetrode position and changes in SC between condition pairs. Each cross
1224 corresponds to average data of a single tetrode. Blue curve, linear regression; red curve,
1225 quadratic polynomial regression. Explained variance (R^2) is indicated with the same color code,
1226 with Pearson correlation coefficient and *P* value provided (54 tetrodes). pro., proximal end; dis.,
1227 distal end.
1228 **d**, Similar to **b** but showing changes in RD across CA1 subdivisions. ***: $P < 0.001$.
1229 **e**, Similar to **c** but showing correlations between tetrode position and changes in RD between
1230 condition pairs.
1231 **f**, PVCs of all putative pyramidal neurons recorded from each subregion in the same room (top
1232 row) and between rooms (middle row), and changes in PVC between room pairs (bottom row)
1233 in the two-room task. Heatmap bins correspond to spatial bins in rate maps. Color scale is
1234 indicated at bottom right.
1235 **g**, Similar to **b** but showing changes in PVC across CA1 bands. Changes in PVC declined
1236 gradually from pCA1 to dCA1. ***: $P < 0.001$.
1237 **h**, Scatter plot showing Pearson correlation between spatial information scores across recording
1238 rooms. Each dot represents data from individual place cells. Neurons located in pCA1, mCA1
1239 and dCA1 are color coded. Dashed line indicates diagonal line. Pearson correlation coefficient
1240 and *P* value are indicated.
1241 **i**, **j**, Similar to **h** but showing correlations between mean spatial information scores and changes
1242 in SC (**i**) and RD (**j**). Dashed line: linear regression.
1243
1244 **Fig 4: Reorganized CA1 population activity to familiar objects.**
1245 **a**, Representative neurons from proximal, middle, and distal bands of CA1, showing responses
1246 to familiar objects placed in the recording box. Maps for the same cell across four trials are
1247 arranged in rows, with animal and cell IDs indicated on the left. Color is scaled to maximum
1248 peak rate of four trials. Text above each map indicates peak rate of that trial. Circles represent

objects. Obj−, trial without objects; Obj+, trial with two familiar objects. Many neurons reorganized their firing activity in response to familiar objects. Note, in pCA1, neuron R0388-T09C1 showed rate redistribution in receptive field away from familiar objects.

b, Distribution of cells in response to object placement across three CA1 bands. Place cells in which receptive fields relocated or appeared/disappeared were first identified, with the remaining cells then grouped according to their RD scores: stable, RD ≤ 0.2, rate-remapped, RD > 0.2. Numbers indicate active place cells in each category. Proportion of rate-remapped cells: chi-square test, $\chi^2 = 1.512$, $P = 0.474$. Proportion of cells in which receptive field appeared/disappeared: *: $P < 0.05$; **: $P < 0.01$.

c, Distribution of PVC in CA1 bands between trials with familiar objects (Same, trial 2 vs trial 3) and trials before and after object placement (+/− obj, trial 1 vs trial 2) for all spatial bins. Horizontal line indicates median, and thick vertical bar indicates IQR of each subregion. Boxplots on the right show changes in PVC between condition pairs, with outliers omitted. ***: $P < 0.001$.

d, PVCs of all putative pyramidal neurons recorded from each subregion between trials with or without objects (top two rows), as well as changes in PVC between condition pairs (bottom row). Heatmap bins correspond to spatial bins in rate maps. Color scales are indicated on the right of each row. Small circles represent objects, large circles indicate object region. Population activity reorganized most robustly in response to the object on the right (bins around left vs right object, Mann-Whitney U tests, all $P < 0.001$), likely due to frequent alterations to this object in the other two object-related tasks.

e, **f**, Distributions of SC (top), RD (middle), and PVC (bottom) within (**e**) and outside (**f**) the object region in CA1 bands between trials with familiar objects (Same) and trials before and after object placement (+/− obj). Horizontal line indicates median, and thick vertical bar indicates IQR of each subregion. Box plots show changes in activity measures between condition pairs, with outliers omitted. *: $P < 0.05$; **: $P < 0.01$; ***: $P < 0.001$.

Fig. 5: Minimum activity change to object relocation in pCA1.

a, Representative neurons in proximal, middle, and distal bands of CA1, showing responses to object displacement. Maps for the same cell across four trials are arranged in rows, with animal

1279 and cell IDs indicated on the left. Color is scaled to maximum peak rate of four trials. Text
1280 above each map indicates peak rate of that trial. Circles represent objects. Fam, objects in
1281 familiar locations; Reloc, trial with right object relocated. New receptive fields emerged around
1282 translocated object in many place cells.
1283 **b**, Distribution of neurons in response to object translocation across three CA1 bands. Place
1284 cells in which receptive fields relocated or appeared/disappeared were first identified, with the
1285 remaining cells then grouped according to their RD scores: stable, RD ≤ 0.2, rate-remapped,
1286 RD > 0.2. Numbers indicate active place cells in each category. Proportion of rate-remapped
1287 cells: chi-square test, χ^2 = 3.624, P = 0.162. Proportion of cells in which receptive field
1288 appeared/disappeared: χ^2 = 14.257, P = 0.001; *post hoc* tests, *: $P < 0.05$; ***: $P < 0.001$.
1289 **c**, Left: distribution of SC in CA1 subregions between trials with relocated objects (Same, trial
1290 2 vs trial 3) and trials before and after object relocation (Moved, trial 1 vs trial 2). Horizontal
1291 line indicates median, and thick vertical bar indicates IQR of each subregion. Right: change in
1292 SC between condition pairs, with outliers omitted. **: $P < 0.01$.
1293 **d**, Correlation between recording position and changes in SC between condition pairs. Each
1294 cross corresponds to average data of a single tetrode. Blue curve, linear regression; red curve,
1295 quadratic polynomial regression. Explained variance (R^2) is indicated with the same color code,
1296 with Pearson correlation coefficient and P value provided. pro., proximal end; dis., distal end.
1297 **e**, Similar to **c** but showing changes in RD across CA1 subdivisions. *: $P < 0.05$.
1298 **f**, Similar to **d** but showing correlations between tetrode position and changes in RD between
1299 condition pairs.
1300 **g**, Similar to **c** but showing changes in PVC across CA1 bands. ***: $P < 0.001$.
1301 **h**, Left panel: PVCs of all putative pyramidal neurons recorded from each subregion between
1302 trials (top two rows), as well as changes in PVC between trial pairs (bottom row) in object-
1303 relocation task. Heatmap bins correspond to spatial bins in rate maps. Color scales are indicated
1304 on the right of each row. Small circles represent objects, large circles indicate target region.
1305 Right panel: changes in PVC inside and outside the target region between trial pairs across CA1
1306 bands, with outliers omitted. *: $P < 0.05$; ***: $P < 0.001$.
1307
1308 **Fig. 6: Elevated sensitivity to novel object in dCA1.**

a, Representative neurons in proximal, middle, and distal bands of CA1, showing remapping to the novel object. Maps of the same cell across four trials are arranged in rows, with animal and cell IDs indicated on the left. Color is scaled to maximum peak rate of four trials. Text above each map indicates peak rate of that trial. Circle and star represent familiar and novel objects, respectively. Fam, trial with two familiar objects; Nov, trial with right object replaced with a novel object. Some neurons exhibited local changes in firing rate around the novel object.

b, Distribution of neurons in response to the novel object across three CA1 bands. Place cells in which receptive fields relocated or appeared/disappeared were first identified, with the remaining cells then grouped according to their RD scores: stable, RD ≤ 0.2, rate-remapped, RD > 0.2. Numbers indicate active place cells in each category. Proportion of rate-remapped cells: chi-square test, $\chi^2 = 0.752$, $P = 0.685$. Proportion of cells in which receptive field appeared/disappeared: $\chi^2 = 24.973$, $P < 0.001$; *post hoc* tests, *: $P < 0.05$; ***: $P < 0.001$.

c, **d**, Left: distributions of SC (**c**) and RD (**d**) in CA1 subregions between trials with a novel object (Same, trial 2 vs trial 3) and trials before and after object replacement (F/N obj, trial 1 vs trial 2). Horizontal line indicates median, and thick vertical bar indicates IQR of each subregion. Right: changes in activity measures between condition pairs, with outliers omitted. *: $P < 0.05$; ***: $P < 0.001$.

e, Correlation between tetrode position and changes in RD between condition pairs. Each cross corresponds to average data of a single tetrode. Blue curve, linear regression; red curve, quadratic polynomial regression. Explained variance (R^2) is indicated with the same color code, with Pearson correlation coefficient and *P* value provided. pro., proximal end; dis., distal end.

f, Similar to **c** but showing changes in PVC across CA1 bands. **: $P < 0.01$; ***: $P < 0.001$.

g, Left panel: PVCs of all putative pyramidal neurons recorded from each subregion between trials (top two rows), as well as changes in PVC between trial pairs (bottom row) in the novel-object task. Heatmap bins correspond to spatial bins in rate maps. Color scales are indicated on the right of each row. Small circle and star represent familiar and novel objects, respectively; large circle indicates region of the novel object. Right panel: changes in PVC inside and outside region of interest between trial pairs across CA1 bands, with outliers omitted. n.s. not significant; ***: $P \leq 0.001$.

1339 **Fig. 7: Independent neuronal responses in related tasks.**

1340 **a**, Representative neurons showing responses to cue manipulation in both color-reversal and
1341 object-placement tasks. Maps of the same cell across four trials in both tasks are arranged in
1342 rows, with animal and cell IDs indicated on the left. Maximum SC between tasks is indicated
1343 under cell ID. Color is scaled to maximum peak rate of four trials for each task. Text above
1344 each map indicates peak rate of that trial. Circle represents familiar object. B, black; W, white
1345 version of the same box. Obj−, trial without objects; Obj+, trial with two familiar objects. Note,
1346 some neurons redistributed their firing rates in both tasks, whereas others only exhibited activity
1347 change in one task.

1348 **b**, Distributions of RD in CA1 neurons recorded in both tasks. For object-placement task, rate
1349 changes outside the object region are shown. Horizontal line indicates median, and thick
1350 vertical bar indicates IQR of each subregion. Dashed line indicates threshold for responsiveness
1351 to cue changes.

1352 **c**, Venn diagram of number and proportion of cells showing rate remapping and indirect
1353 response cue changes in color-reversal and object-placement tasks, respectively. Number in red
1354 indicates expected overlap. n.s., not significant.

1355 **d**, Scatter plot showing changes in RD in color-reversal and object-placement tasks. Each dot
1356 represents data from an individual place cell. Neurons located in pCA1, mCA1, and dCA1 are
1357 color coded.

1358 **e**, Similar to **a** but showing representative neurons responding to object feature changes in
1359 object-relocation and novel-object tasks. Circle and star represent familiar and novel objects,
1360 respectively. Fam, trial with two familiar objects in familiar locations; Reloc, trial with right
1361 object relocated. Nov, trial with right object replaced with a novel object. Note, some neurons
1362 (R0172-T08C1, R0175-T16C1, R1028-T03C1) reorganized their activities in both tasks but in
1363 different forms.

1364 **f**–**h**, Similar to **b**–**e** but showing data from the population of place cells recorded in both the
1365 object-relocation and novel-object tasks.

1366

1367 **Fig. 8: Summary of findings and afferent connections that varied along CA1 transverse**
1368 **axis.**

Top: three distinct patterns of cue representation that varied along CA1 proximodistal axis. Bottom: projection profiles to CA1 within hippocampal region, with reported regional functions indicated.

Fig. 1

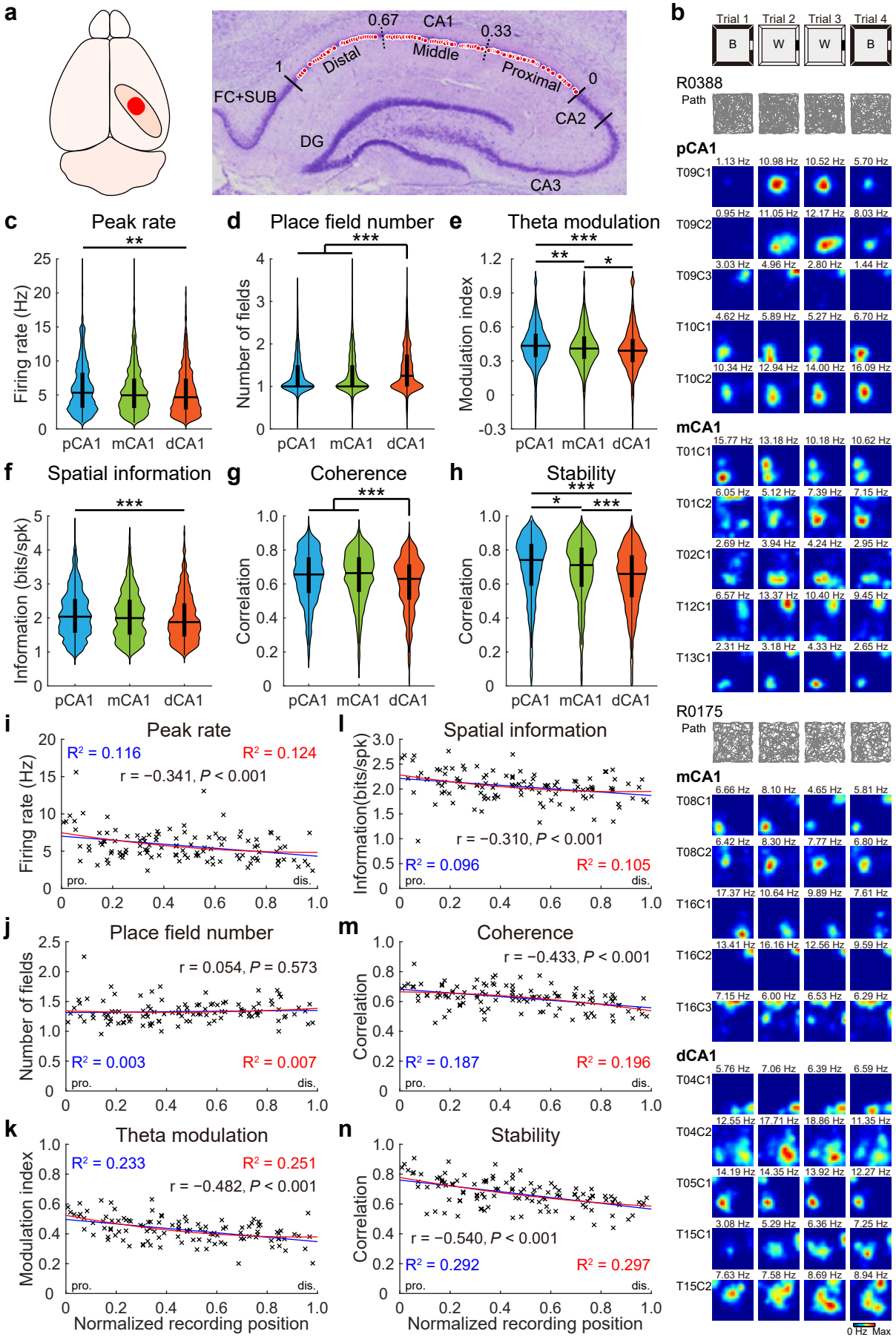
a
0.67
CA1
0.33
1
Distal
Middle
Proximal
0
FC+SUB
CA2
DG
CA3
b
Trial 1
Trial 2
Trial 3
Trial 4
B
W
W
B
R0388
Path
pCA1
T09C1
T09C2
T09C3
T10C1
T10C2
mCA1
T01C1
T01C2
T02C1
T12C1
T13C1
R0175
Path
mCA1
T08C1
T08C2
T16C1
T16C2
T16C3
dCA1
T04C1
T04C2
T05C1
T15C1
T15C2
0 Hz
Max
c
Peak rate
Firing rate (Hz)
pCA1
mCA1
dCA1
d
Place field number
Number of fields
e
Theta modulation
Modulation index
f
Spatial information
Information (bits/spk)
g
Coherence
Correlation
h
Stability
Correlation
i
Peak rate
Firing rate (Hz)
R² = 0.116
R² = 0.124
r = −0.341, P < 0.001
pro.
dis.
l
Spatial information
Information(bits/spk)
r = −0.310, P < 0.001
R² = 0.096
R² = 0.105
j
Place field number
Number of fields
r = 0.054, P = 0.573
R² = 0.003
R² = 0.007
m
Coherence
Correlation
r = −0.433, P < 0.001
R² = 0.187
R² = 0.196
k
Theta modulation
Modulation index
R² = 0.233
R² = 0.251
r = −0.482, P < 0.001
n
Stability
Correlation
r = −0.540, P < 0.001
R² = 0.292
R² = 0.297
Normalized recording position
Normalized recording position

Fig. 2

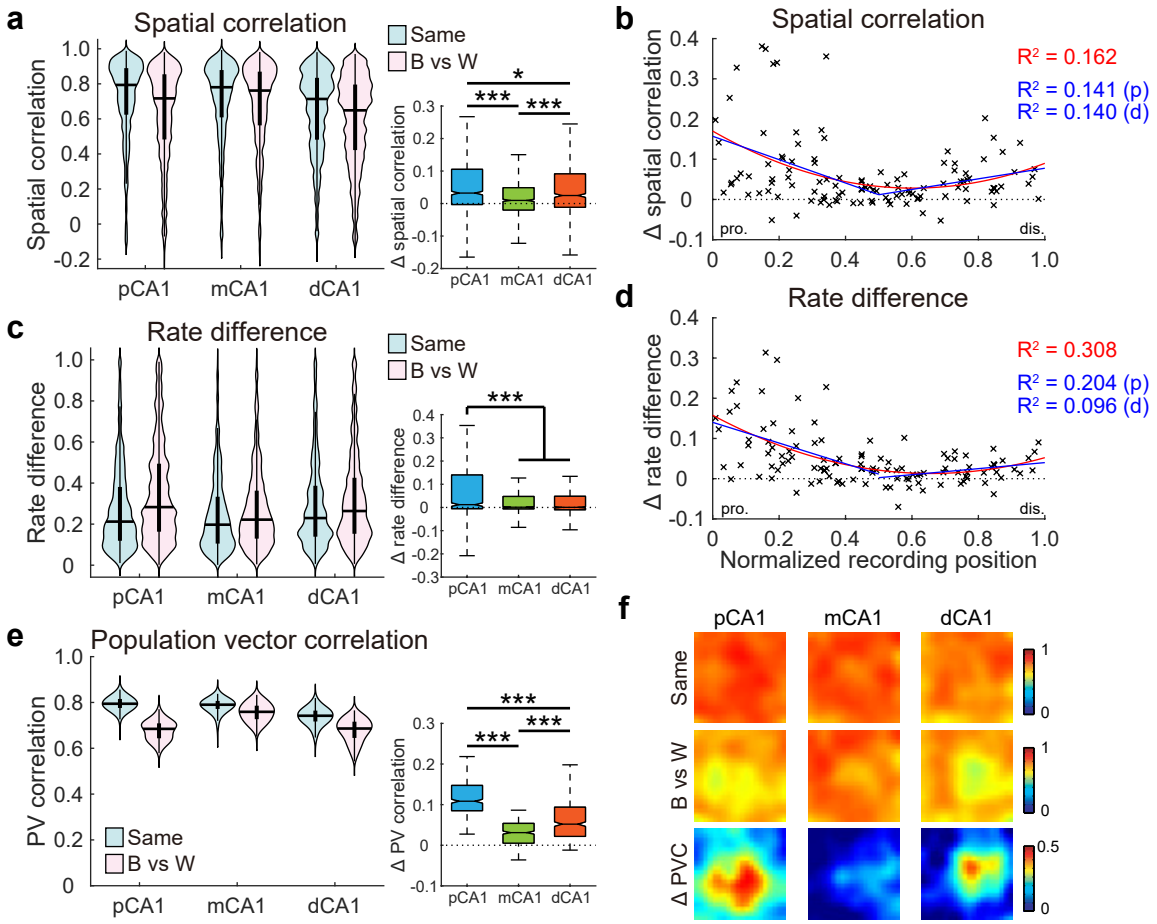
a
Spatial correlation
Spatial correlation
Same
B vs W
Δ spatial correlation
pCA1
mCA1
dCA1
b
Spatial correlation
Δ spatial correlation
R² = 0.162
R² = 0.141 (p)
R² = 0.140 (d)
pro.
dis.
c
Rate difference
Rate difference
Δ rate difference
d
Rate difference
Δ rate difference
R² = 0.308
R² = 0.204 (p)
R² = 0.096 (d)
Normalized recording position
e
Population vector correlation
PV correlation
Δ PV correlation
f
Same
B vs W
Δ PVC

Fig. 3

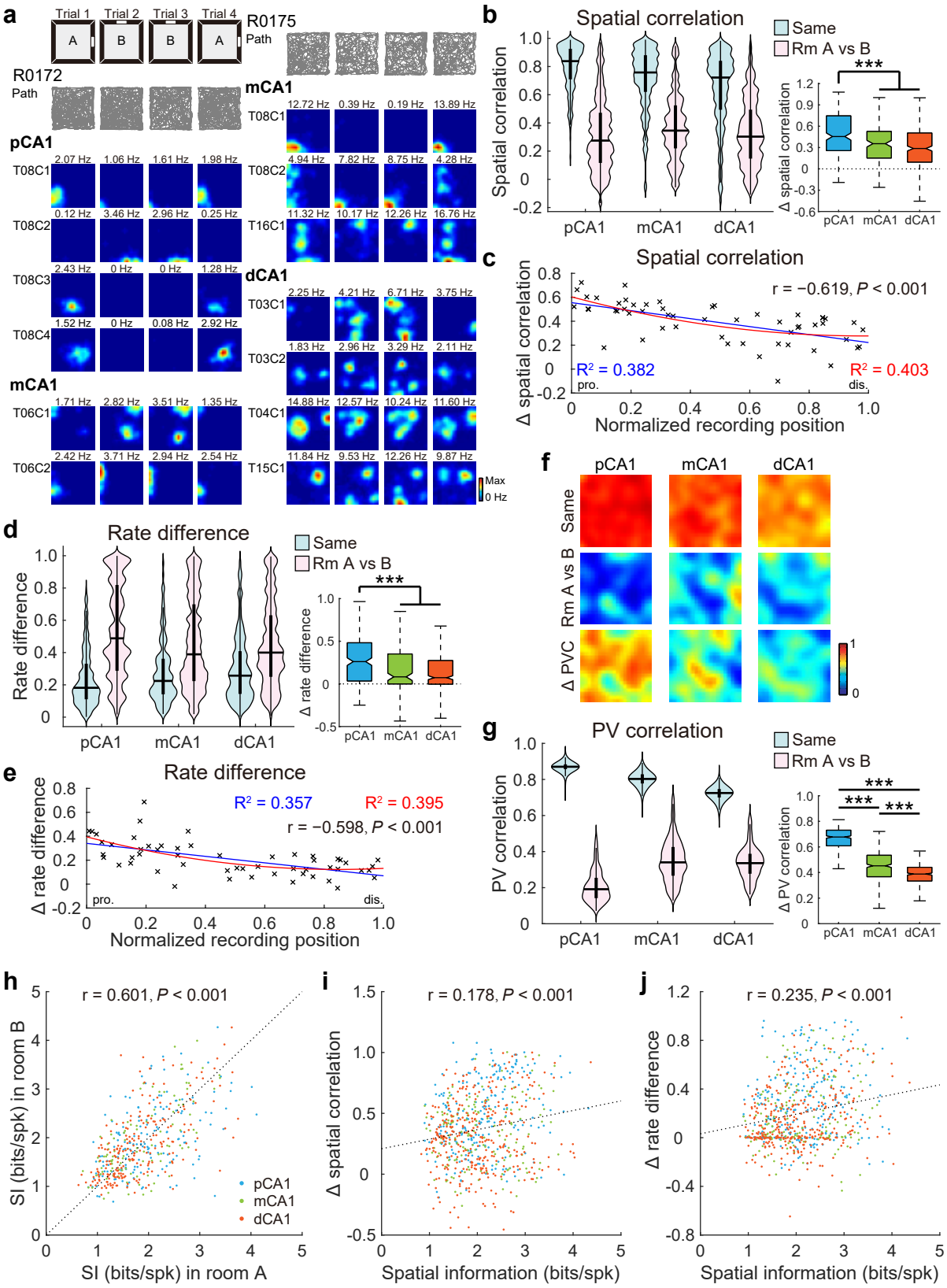
a
Trial 1
Trial 2
Trial 3
Trial 4
A
B
B
A
R0172
Path
R0175
Path
pCA1
mCA1
dCA1
T08C1
T08C2
T08C3
T08C4
T06C1
T06C2
T16C1
T03C1
T03C2
T04C1
T15C1
Max
0 Hz
b
Spatial correlation
Same
Rm A vs B
Spatial correlation
Δ spatial correlation
pCA1
mCA1
dCA1
***
c
Spatial correlation
r = −0.619, P < 0.001
R² = 0.382
R² = 0.403
pro.
dis.
Δ spatial correlation
Normalized recording position
d
Rate difference
Same
Rm A vs B
Rate difference
Δ rate difference
pCA1
mCA1
dCA1
***
e
Rate difference
R² = 0.357
R² = 0.395
r = −0.598, P < 0.001
pro.
dis.
Δ rate difference
Normalized recording position
f
pCA1
mCA1
dCA1
Same
Rm A vs B
Δ PVC
g
PV correlation
Same
Rm A vs B
PV correlation
Δ PV correlation
pCA1
mCA1
dCA1
***
h
r = 0.601, P < 0.001
SI (bits/spk) in room B
SI (bits/spk) in room A
pCA1
mCA1
dCA1
i
r = 0.178, P < 0.001
Δ spatial correlation
Spatial information (bits/spk)
j
r = 0.235, P < 0.001
Δ rate difference
Spatial information (bits/spk)

Fig. 4

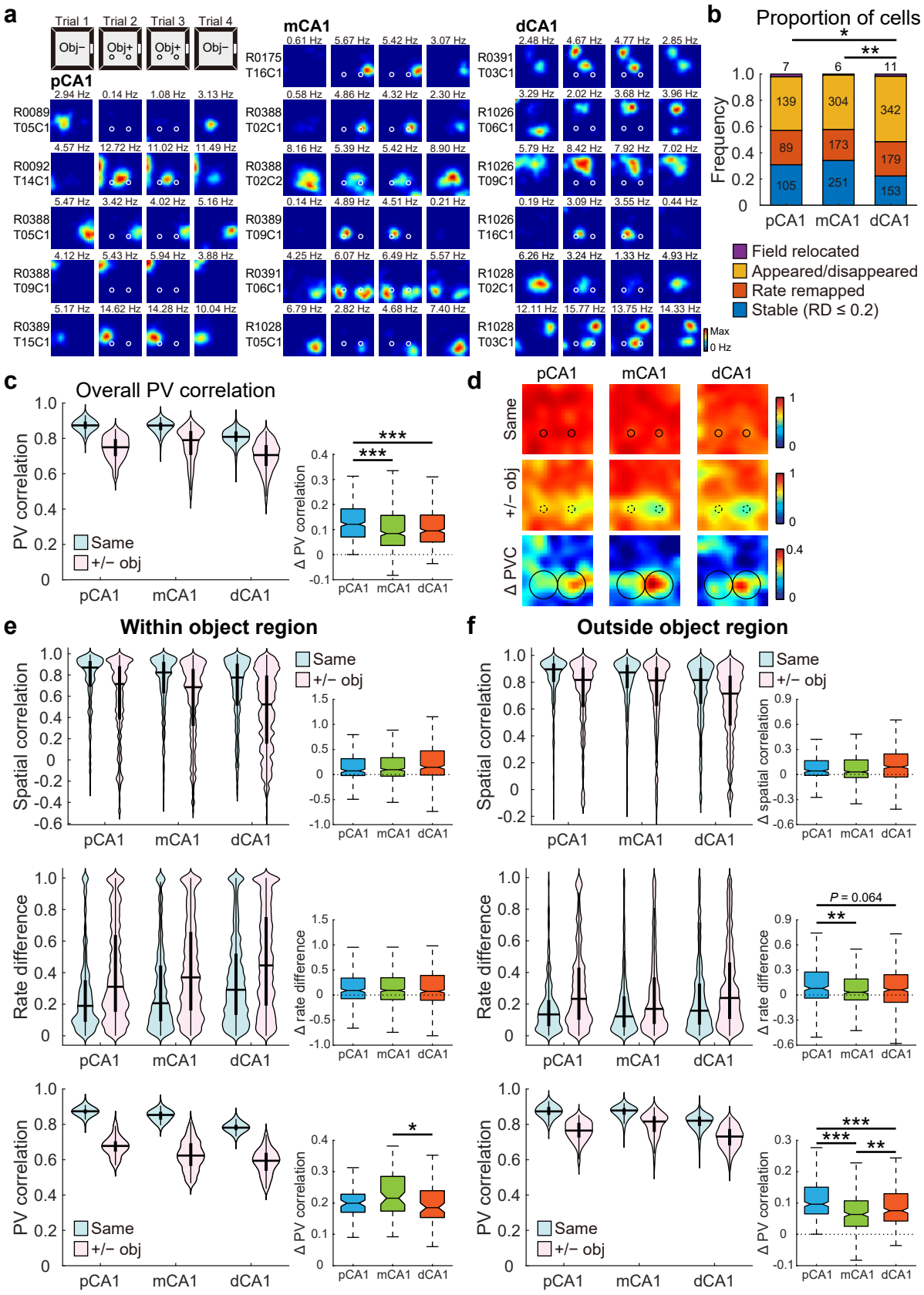
a
Trial 1
Trial 2
Trial 3
Trial 4
Obj−
Obj+
Obj+
Obj−
pCA1
mCA1
dCA1
R0089 T05C1
R0092 T14C1
R0388 T05C1
R0388 T09C1
R0389 T15C1
R0175 T16C1
R0388 T02C1
R0388 T02C2
R0389 T09C1
R0391 T06C1
R1028 T05C1
R0391 T03C1
R1026 T06C1
R1026 T09C1
R1026 T16C1
R1028 T02C1
R1028 T03C1
Max
0 Hz
b
Proportion of cells
Frequency
pCA1
mCA1
dCA1
Field relocated
Appeared/disappeared
Rate remapped
Stable (RD ≤ 0.2)
c
Overall PV correlation
PV correlation
Same
+/− obj
Δ PV correlation
d
Same
+/− obj
Δ PVC
e
Within object region
Spatial correlation
Rate difference
PV correlation
Δ spatial correlation
Δ rate difference
Δ PV correlation
f
Outside object region
P = 0.064

Fig. 5

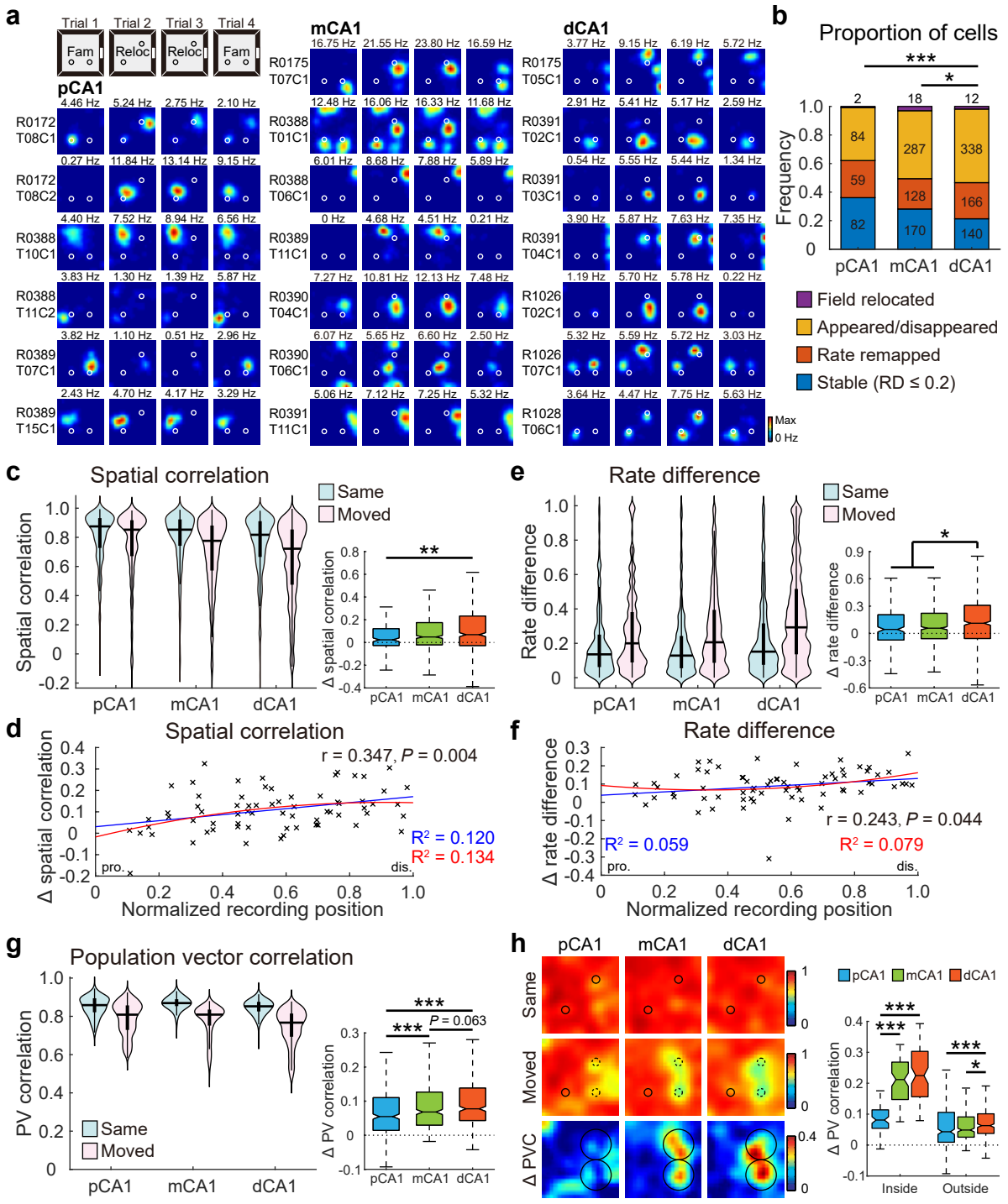
a
Trial 1
Trial 2
Trial 3
Trial 4
Fam
Reloc
Reloc
Fam
pCA1
mCA1
dCA1
R0172 T08C1
R0172 T08C2
R0388 T10C1
R0388 T11C2
R0389 T07C1
R0389 T15C1
R0175 T07C1
R0388 T01C1
R0388 T06C1
R0389 T11C1
R0390 T04C1
R0390 T06C1
R0391 T11C1
R0175 T05C1
R0391 T02C1
R0391 T03C1
R0391 T04C1
R1026 T02C1
R1026 T07C1
R1028 T06C1
Max
0 Hz
b
Proportion of cells
Frequency
Field relocated
Appeared/disappeared
Rate remapped
Stable (RD ≤ 0.2)
c
Spatial correlation
Same
Moved
Δ spatial correlation
d
Spatial correlation
r = 0.347, P = 0.004
R² = 0.120
R² = 0.134
pro.
dis.
Normalized recording position
e
Rate difference
Δ rate difference
f
Rate difference
r = 0.243, P = 0.044
R² = 0.059
R² = 0.079
g
Population vector correlation
PV correlation
Δ PV correlation
P = 0.063
h
Δ PVC
Inside
Outside

Fig. 6

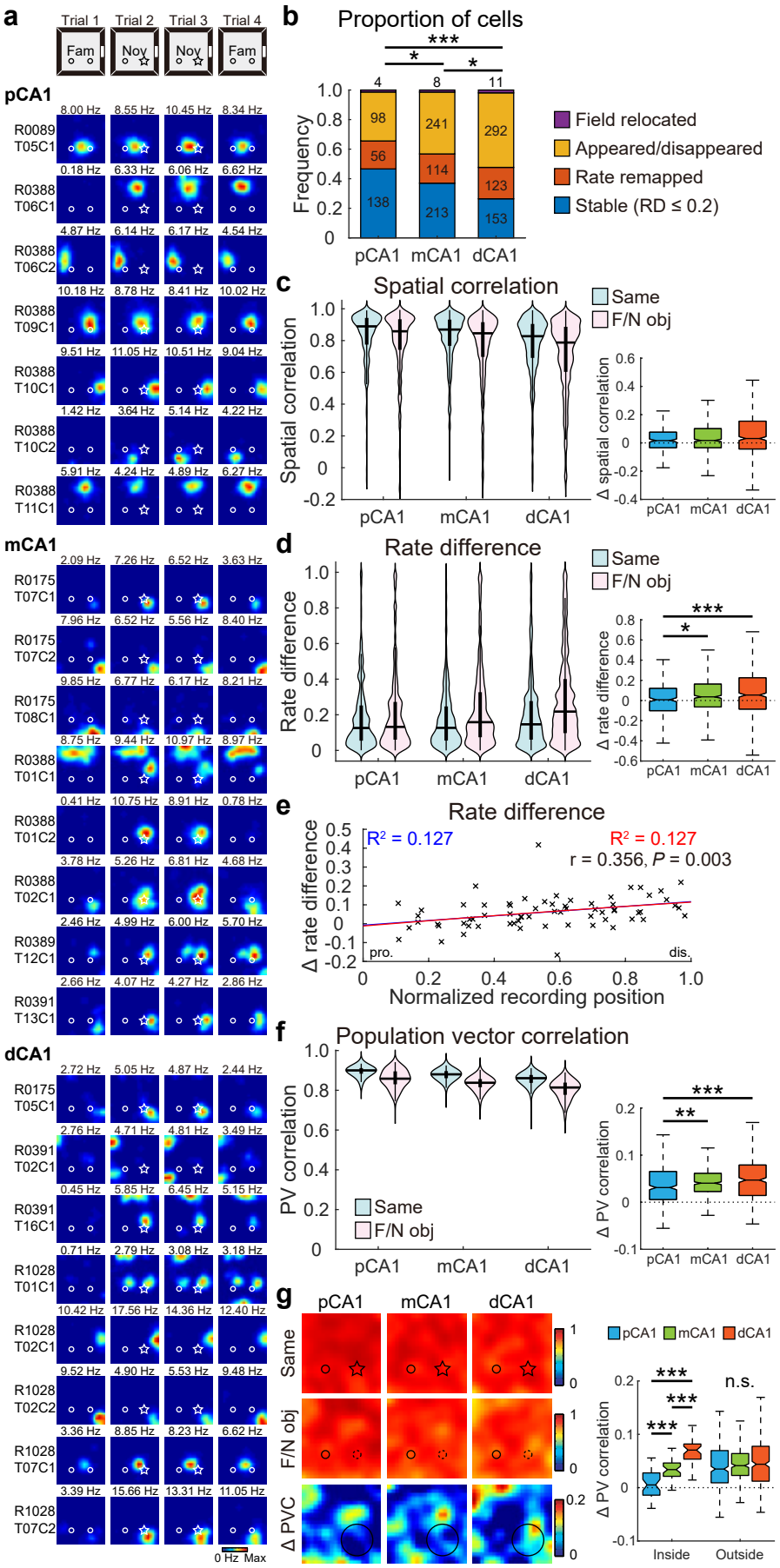
a
Trial 1
Trial 2
Trial 3
Trial 4
Fam
Nov
Nov
Fam
pCA1
mCA1
dCA1
0 Hz Max
b
Proportion of cells
Frequency
Field relocated
Appeared/disappeared
Rate remapped
Stable (RD ≤ 0.2)
pCA1 mCA1 dCA1
c
Spatial correlation
Same
F/N obj
Spatial correlation
Δ spatial correlation
d
Rate difference
Rate difference
Δ rate difference
e
Rate difference
R² = 0.127
R² = 0.127
r = 0.356, P = 0.003
Δ rate difference
pro.
dis.
Normalized recording position
f
Population vector correlation
PV correlation
Δ PV correlation
g
Same
F/N obj
Δ PVC
Δ PV correlation
Inside
Outside
n.s.

Fig. 7

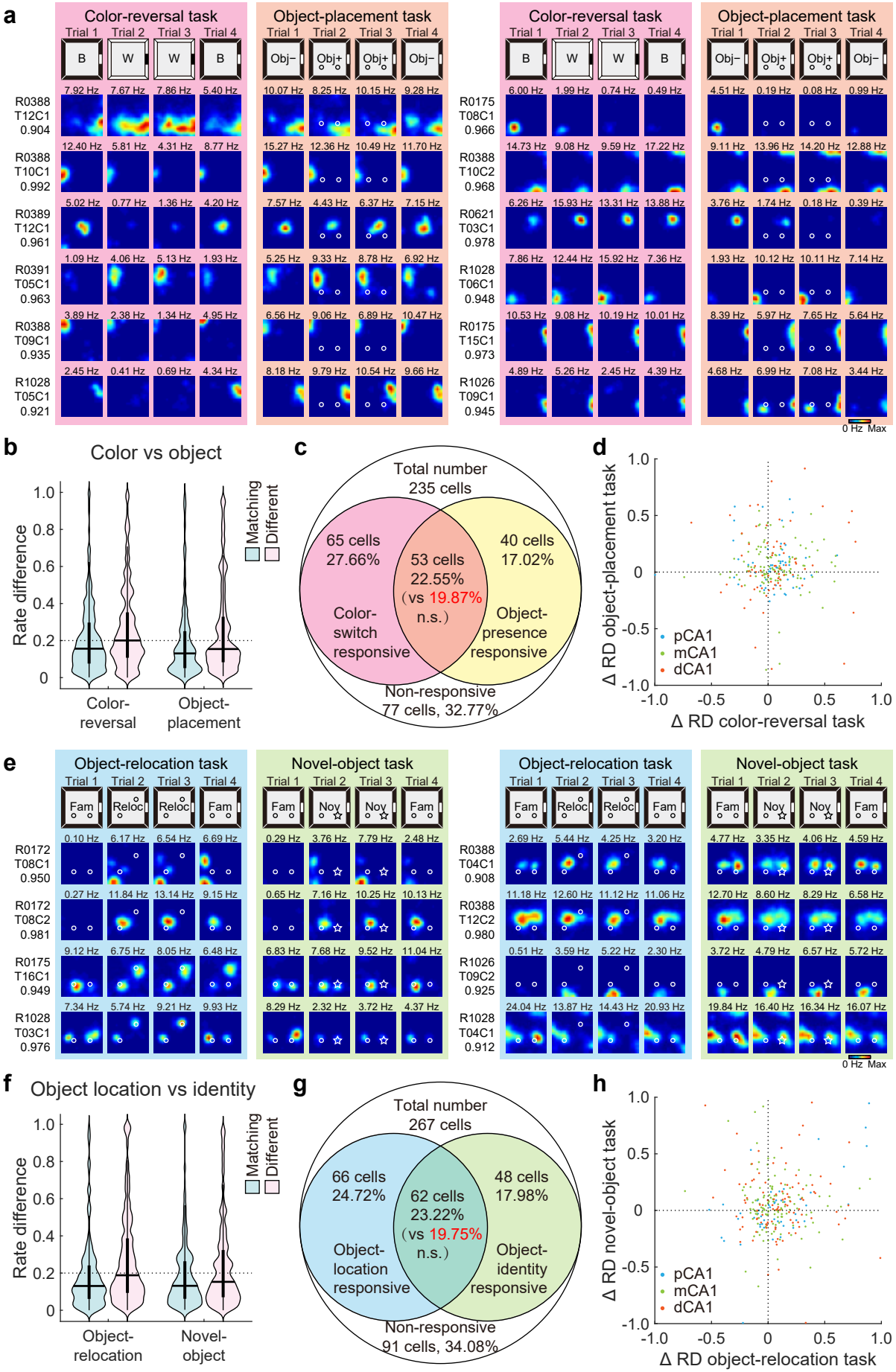
a
Color-reversal task
Object-placement task
Trial 1
Trial 2
Trial 3
Trial 4
B
W
Obj−
Obj+
R0388 T12C1 0.904
R0388 T10C1 0.992
R0389 T12C1 0.961
R0391 T05C1 0.963
R0388 T09C1 0.935
R1028 T05C1 0.921
R0175 T08C1 0.966
R0388 T10C2 0.968
R0621 T03C1 0.978
R1028 T06C1 0.948
R0175 T15C1 0.973
R1026 T09C1 0.945
0 Hz Max
b
Color vs object
Rate difference
Matching
Different
Color-reversal
Object-placement
c
Total number 235 cells
65 cells 27.66%
53 cells 22.55% (vs 19.87% n.s.)
40 cells 17.02%
Color-switch responsive
Object-presence responsive
Non-responsive 77 cells, 32.77%
d
Δ RD object-placement task
Δ RD color-reversal task
pCA1
mCA1
dCA1
e
Object-relocation task
Novel-object task
Fam
Reloc
Nov
R0172 T08C1 0.950
R0172 T08C2 0.981
R0175 T16C1 0.949
R1028 T03C1 0.976
R0388 T04C1 0.908
R0388 T12C2 0.980
R1026 T09C2 0.925
R1028 T04C1 0.912
0 Hz Max
f
Object location vs identity
Rate difference
Matching
Different
Object-relocation
Novel-object
g
Total number 267 cells
66 cells 24.72%
62 cells 23.22% (vs 19.75% n.s.)
48 cells 17.98%
Object-location responsive
Object-identity responsive
Non-responsive 91 cells, 34.08%
h
Δ RD novel-object task
Δ RD object-relocation task
pCA1
mCA1
dCA1

Fig. 8

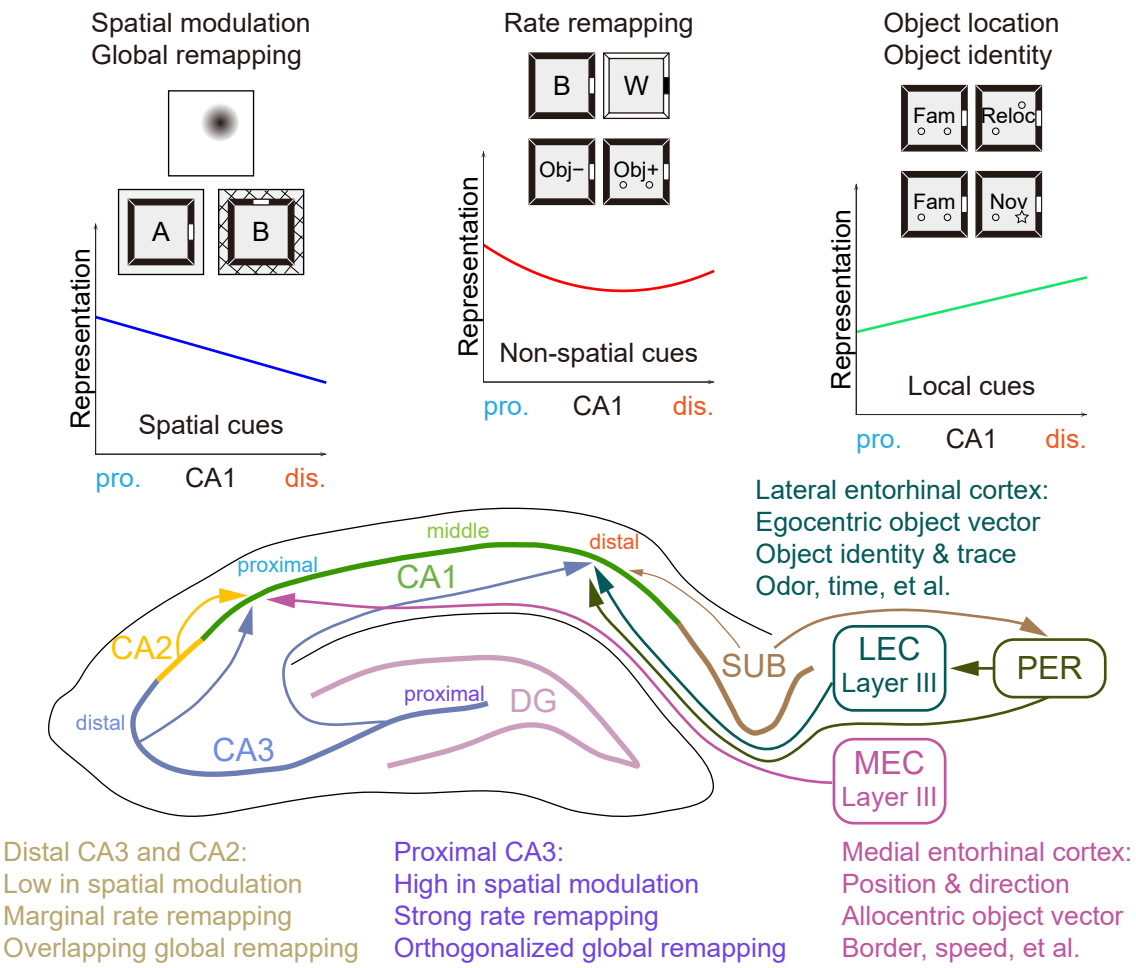

Distal CA3 and CA2:
Low in spatial modulation
Marginal rate remapping
Overlapping global remapping

Proximal CA3:
High in spatial modulation
Strong rate remapping
Orthogonalized global remapping

Medial entorhinal cortex:
Position & direction
Allocentric object vector
Border, speed, et al.